Retrieving cloud, dust and ozone abundances in the Martian atmosphere using SPICAM/UV nadir spectra

Y. Willame, A. C. Vandaele, C. Depiesse, Franck Lefèvre, V. Letocart, D. Gillotay, Franck Montmessin

Planetary and Space Science xxx (xxxx) xxx–xxx

Contents lists available at ScienceDirect

Planetary and Space Science

journal homepage: www.elsevier.com/locate/pss

Retrieving cloud, dust and ozone abundances in the Martian atmosphere using SPICAM/UV nadir spectra

Y. Willame[a,*], A.C. Vandaele[a], C. Depiesse[a], F. Lefèvre[b], V. Letocart[a], D. Gillotay[a], F. Montmessin[b]

[a] Institut Royal d'Aéronomie Spatiale de Belgique, 3 av. circulaire, 1180 Bruxelles, Belgium
[b] Laboratoire Atmosphères Milieux Observations Spatiales, Paris, France

ARTICLE INFO

Keywords:
Mars atmosphere
Nadir retrieval
Cloud
Dust
Ozone
SPICAM/UV

ABSTRACT

We present the retrieval algorithm developed to analyse nadir spectra from SPICAM/UV aboard Mars-Express. The purpose is to retrieve simultaneously several parameters of the Martian atmosphere and surface: the dust optical depth, the ozone total column, the cloud opacity and the surface albedo. The retrieval code couples the use of an existing complete radiative transfer code, an inversion method and a cloud detection algorithm. We describe the working principle of our algorithm and the parametrisation used to model the required absorption, scattering and reflection processes of the solar UV radiation that occur in the Martian atmosphere and at its surface. The retrieval method has been applied on 4 Martian years of SPICAM/UV data to obtain climatologies of the different quantities under investigation. An overview of the climatology is given for each species showing their seasonal and spatial distributions. The results show a good qualitative agreement with previous observations. Quantitative comparisons of the retrieved dust optical depths indicate generally larger values than previous studies. Possible shortcomings in the dust modelling (altitude profile) have been identified and may be part of the reason for this difference. The ozone results are found to be influenced by the presence of clouds. Preliminary quantitative comparisons show that our retrieved ozone columns are consistent with other results when no ice clouds are present, and are larger for the cases with clouds at high latitude. Sensitivity tests have also been performed showing that the use of other a priori assumptions such as the altitude distribution or some scattering properties can have an important impact on the retrieval.

1. Introduction

The solar ultraviolet radiation can be used to study several key elements in the Martian atmosphere such as dust, ice clouds and ozone. Airborne dust is ubiquitous in the Martian atmosphere. It highly influences Martian climate due to its absorption of solar radiation, resulting in a local warming of the atmosphere. The monitoring of the dust cycle shows two main periods along the Martian year: the "cold" aphelion season where dust concentration is relatively low and usually very repeatable from one year to another (Smith, 2009); and the "warm" perihelion, where the dust loading is higher and characterised by frequent dust storms. These storms occur randomly in time with various size going from local storms to planetary events, inducing a larger variability during that period (Smith, 2008). Size, shape and scattering properties of Martian dust were studied using groundbased and remote observations (e.g. Tomasko et al., 1999; Clancy et al., 2003; Wolff et al., 2009, 2010). Dust particles also serve as condensation nuclei for ice cloud formation.

Ice clouds play an important role in the Martian climate and are related to the water vapour cycle. They were shown to induce an asymmetry in the transport of water vapour from one hemisphere to the other (Clancy et al., 1996). They usually appear under situation of adiabatically cooled upward flows where the water vapour condenses on dust particles. The observation of clouds allowed to study their seasonal, spatial and even day-night distribution showing that clouds were observed under several forms: the equatorial cloud belt arising during cold aphelion (Smith, 2004, 2009), polar hoods that covers the poles of the winter hemisphere (Benson et al., 2010, 2011) and orographic clouds found above the tallest volcanoes (Benson et al., 2003, 2006). Ice clouds properties such as particle size and shape were also deduced from EPF observations, showing that there was two types of clouds (Clancy et al., 2003): type 1, which has a particle size of 1–2 μm, and is frequently observed in the southern hemisphere around aphelion but also above orographic heights and as altitude clouds; while type 2 has a 3–4 μm size and is observed in the aphelion cloud belt.

Ozone, which is an important UV absorber, is a very reactive species in the Martian atmosphere. It is produced through the photolysis of CO_2

* Corresponding author.
E-mail address: yannick.willame@aeronomie.be (Y. Willame).

http://dx.doi.org/10.1016/j.pss.2017.04.011
Received 25 November 2016; Received in revised form 13 April 2017; Accepted 15 April 2017

and O_2 that releases O atoms which recombine with O_2 to form the ozone molecule. The ozone abundance is anti-correlated with that of water vapour as the depletion of ozone is mainly due to the presence of odd hydrogen species HO_x which are produced by the water vapour photo-dissociation (Lefèvre et al., 2004, 2008). Ozone is known to be present at high concentration from mid-to-high latitudes above the winter pole (up to 40 μm-atm), where the water vapour has condensed on the polar cap. The mid-to-high latitude ozone shows a large variability along the seasons as its quantities strongly decreases to 1–4 μm-atm during the summer (Perrier et al., 2006; Clancy et al., 2016). The high latitude ozone trapped in the polar vortex during winter, was recently shown to be a tracer to observe the dynamics of the vortex waves (Clancy et al., 2016). On the contrary, at low-to-mid latitude, the ozone concentration is more constant and remains in relatively low quantities: low quantities around 1 μm-atm are generally observed with noticeable increase up to 2–3 μm-atm around aphelion (Perrier et al., 2006; Clancy et al., 2016). That increase is related to the low altitude level of water vapour due to low temperature, allowing an altitude ozone layer to develop above 10–20 km (Lefèvre et al., 2004).

Several instruments have been used to monitor one or more of these three species, among the most recent ones we find: MOC and TES aboard MGS; THEMIS on Mars Odyssey; OMEGA, PFS and SPICAM on Mars-Express; Pancam on the MER; and MCS, CRISM or MARCI from MRO. SPICAM is one of the instruments on board Mars-Express (MEX), orbiting around Mars since the very end of 2003. The SPICAM instrument is a spectrometer composed of two channels operating in the infrared and ultraviolet (UV) respectively. Works using SPICAM/UV have provided climatologies for the beginning of the mission: ozone for the first 1.2 Martian years (Perrier et al., 2006), and ice clouds for the first 2.2 MY (Mateshvili et al., 2007b, 2009).

In this paper, we present an improved retrieval algorithm developed to quantitatively analyse nadir spectra from SPICAM/UV. It allows to derive simultaneously the total abundance of ozone, dust and ice clouds as well as the surface albedo. The retrieval results can be used to analyse the spatial and seasonal distributions in order to contribute to complete our knowledge about these species and compare with the other existing climatologies. We start with a brief description of the SPICAM instrument and the data used in this work. We describe then the retrieval method that combines the use of the full radiative transfer code LIDORT (Spurr et al., 2001) and the optimal estimation method (Rodgers, 2000). The parametrisation chosen to model the atmosphere uses more recent results than in the previous works, based on SPICAM/UV, of Perrier et al. (2006), Mateshvili et al. (2007b) and Mateshvili et al. (2009). We have performed the analysis of SPICAM/UV data on more than 4 MY and derived climatologies for the retrieved species. An overview of these climatologies is presented, describing the seasonal and spatial trends observed for each parameter. A comparison with climatologies obtained in previous studies is also provided. We also present the results of several sensitivity tests performed to quantify the impact of using different assumptions as the altitude distribution or the scattering properties. We give a comparison between the retrieval results obtained by the present parametrisation and those obtained with the assumptions used in the previous SPICAM/UV works of Perrier et al. (2006), Mateshvili et al. (2007b) and Mateshvili et al. (2009).

2. SPICAM instrument and data

2.1. SPICAM instrument

In the present work, we used the measurements recorded in nadir viewing with the UV channel. SPICAM/UV covers the spectral range from about 118–320 nm with a resolution of 1.5 nm. The light is collected through a slit and recorded by a CCD detector. A measurement consists in 5 "bands" (a band corresponds to the binning of 4 CCD lines) for which each line is composed of 384 illuminated spectral pixels of about 0.55 nm sampling. The nadir footprint of a 5 band scan usually varies within 1–2 km along track and 2–15 km cross track. A detailed description of the SPICAM/UV instrument can be found in Bertaux et al. (2006).

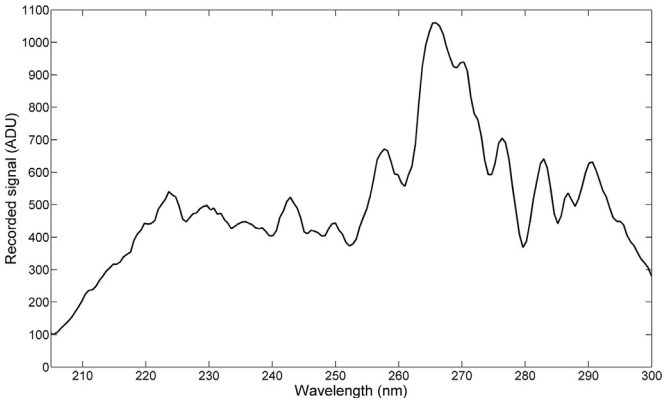

Fig. 1. A typical level 1A nadir measurement in ADU from SPICAM/UV (Orbit 500, measurement 870).

2.2. Data calibration

We have used level 1A data corrected for dark charge non uniformity and reading noise. The data are expressed in ADU (Analog to Digital Unit). An example of level 1A data is shown in Fig. 1. The data are then converted into radiance factors (R_f): $R_f(\lambda) = \pi I(\lambda)/F_S(\lambda)$ where λ is the wavelength, I is the scattered light intensity (radiance) entering the slit and F_S is the solar irradiance at the top of the atmosphere (TOA). The solar fluxes used as references are based upon the public data of the SOLSTICE instrument on board the SORCE satellite.

We also applied a correction to take account of the dispersion of the incident light on the CCD. The method is based on the use of a Point Spreading Function (PSF) which is two dimensional Voigt profile (for spatial and spectral dimension). It was calculated in Marcq et al. (2011) using stellar observations. The R_f spectrum, corresponding to the measurement in Fig. 1, is represented by the grey line in Fig. 3.

2.3. Spectral interval

In order to save calculation time, the retrieval is performed on 8 different wavelengths in the 220–290 nm interval. The interval was chosen in order to work with the most reliable part of the spectra. Below 202 nm, the CO_2 absorbs (almost) completely the incident light. Between 202 and 220 nm, the calibrated R_f is not reproduced by the radiative transfer (RT) calculation. We suspect this discrepancy to be related to the calibration: the effective flux recorded becoming relatively weak makes these intervals more sensitive to inaccuracies in the calibration. Above 290 nm, the instrument sensitivity becomes weak (low values of the response curve) with a larger uncertainty and the calibrated R_f is also not correctly reproduced by the RT calculation (see Fig. 3).

2.4. Binning and uncertainty

In order to increase the signal-to-noise ratio of the radiance factor, data binnings are performed, averaging on several measurements together and on several wavelengths: For the SPICAM data, we use the 5 bands of 9 consecutive measurements and a spectral binning on 9 wavelengths (≈ 5 nm); For the constructed solar spectrum F_S, we use 7–8 consecutive daily SOLSTICE measurements (i.e. 4 F_S per month) and a binning on the spectral interval equivalent to 9 SPICAM wavelengths.

The uncertainty on the radiance factor R_f is calculated from three contributions: 1) The uncertainty on the recorded ADUs which is composed of the shot noise and of the dark charge and electronic noise subtraction error; 2) The uncertainty on F_S, calculated in McClintock et al. (2005), is approximately constant and always <3% in the 200–300 nm interval. In this work, we have used a constant value of 3%; And 3) the uncertainty on the instrument response curve provided by the SPICAM team (using v9 here).

The total uncertainty on the radiance factor in the 220–290 nm interval decreases from around 15–20% for a single band without binning to typically 2–4% when the binning is performed.

2.5. Measurement coverage

In this work, we analysed the 4 first Martian years of SPICAM/UV measurements, going from orbit 61 recorded at L_s= 341° in MY26 to orbit 9821 taken at end of MY30 (using the arbitrary time reference defined in Clancy et al. (2000)). This corresponds to the period before September 2011 when MEX entered in Safe Mode 25 and which was followed by the steep increase of the number of defective spectra. The 4 MY period includes more than 2500 orbits in nadir mode, containing in total more than 4.5 million measurements. The seasonal coverage over the 4 Martian years is given in Fig. 2.

3. Retrieval method

3.1. Retrieval algorithm overview

We describe here the retrieval algorithm which was developed to retrieve atmospheric and surface parameters from SPICAM/UV nadir measurements. The retrieval algorithm is an iterative process which consists in a main program which calls a sequence of different subroutines: a cloud detection algorithm which was specifically developed in order to identify in which measurements clouds have to be taken into account in the retrieval; a full radiative transfer (RT) model used for spectra simulation and for the calculation of the parameters' derivatives; and an inversion method to estimate the best values of the retrieved parameters.

The goal is to deduce the ozone column, the dust and the cloud vertical opacities and the surface albedo from each single SPICAM measurement obtained in nadir geometry. As we retrieve column integrated quantities, the columns are obtained by scaling the *a priori* vertical profile. With the exception of ozone, these parameters correspond to broadband contributions to the radiance factor between 220 and 290 nm, which makes them difficult to decorrelate. We have decided after several tests to only fit 3 parameters simultaneously in order to keep them independent: ozone and dust are always retrieved while cloud is fitted if present, otherwise the surface albedo is the third retrieved parameter. An example of retrieval is shown in Fig. 3.

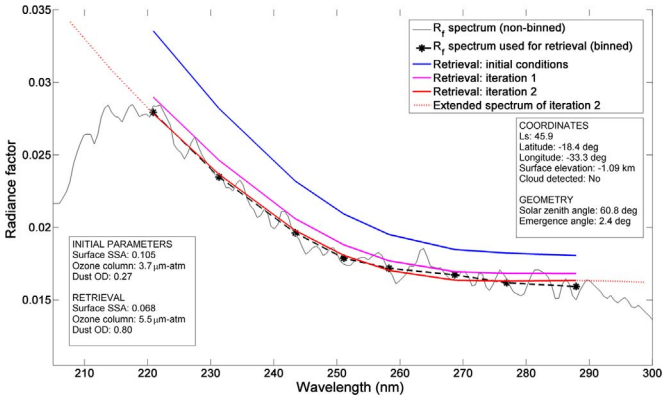

Fig. 3. Example of a spectral inversion performed with the algorithm developed (Orbit 500, measurement 870). The non-binned measured spectrum is represented by a grey line. The binned measured spectrum (MS) used for the retrieval is given in black dashed line with asterisk markers. The initial simulated spectrum (SS) obtained from the *a priori* conditions is represented in blue. The SS obtained after one iteration is given in magenta (RMS = 0.045). The SS obtained after a second iteration is represented in red and has converged (RMS = 0.014). An extended spectrum of iteration 2 is given in red dotted line, showing that the simulation can not reproduce the measurement outside the 220–290 nm range (cf. Section 2.3). (For interpretation of the references to color in this figure legend, the reader is referred to the web version of this article.)

The retrieval procedure is schematised in Fig. 4 and is summarised hereafter in several steps:

1. Cloud detection:
   We start the procedure by applying the cloud detection routine which identifies if the measurement is affected by the presence of a cloud. Clouds appear bright in the UV compared to the dark regolith surface and as Fig. 5 shows, their presence results in a relatively large increase of the recorded signal. More precisely, the increase of signal is proportionally more important at longer wavelengths than at shorter wavelengths in the interval considered (220–290 nm). The principle of detection is based on the combination of two characteristics: a relatively large increase of the averaged signal (S_{av}) and an increase of a longer/shorter wavelength ratio ($R_{l/s}$). This combination allows to differentiate from the effects due to dust, ozone and Rayleigh scattering. However, the surface reflection also shows such a combination. But as the regolith is strongly absorbing and partially occulted by the airborn dust layer, it induces only limited signal variations that can be differentiated by choosing an adapted (large enough) threshold. On the contrary, ice surface is very bright and can not be differentiated by such a threshold. Ice caps, based on the MCD (Mars Climate Database) v5.0 predictions, were therefore excluded in the cloud detection. An "uncertain" area of about 10° latitude is also delimited at the edge of the ice caps. The detections in these uncertain areas are treated by performing two

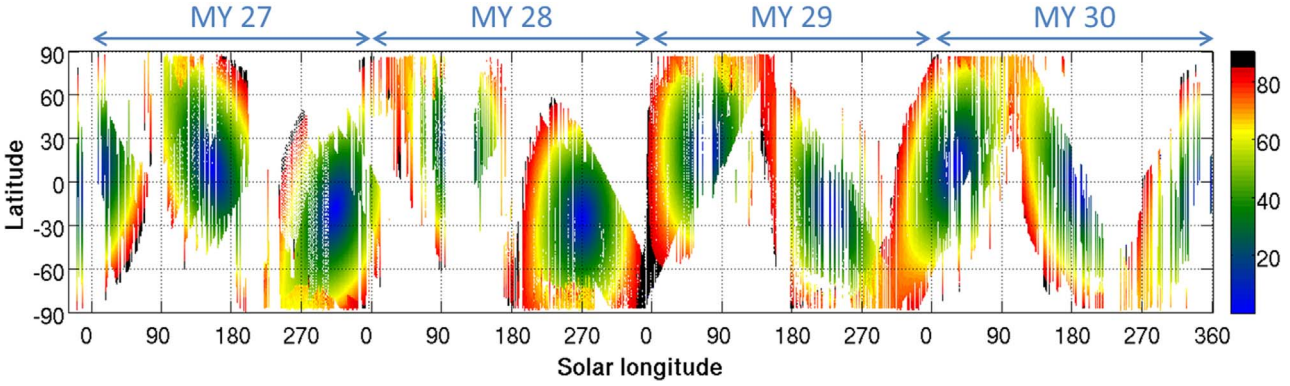

Fig. 2. Latitudinal coverage of SPICAM/UV nadir measurements during Martian years 27–30. The colour scale indicates the solar zenith angle (SZA) at the location and time of measurement. Values of SZA>85° were not considered in the retrievals and are black-coloured.

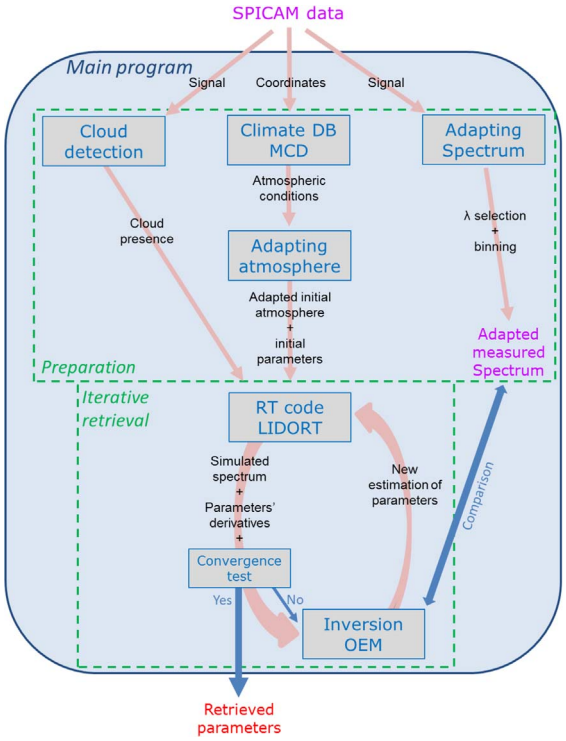

Fig. 4. Schematic of the retrieval procedure.

independent retrievals: one including a cloud (above a regular surface) and a second considering ice surface (and no cloud). The solution with the best fit is then selected.

Practically, each orbit is analysed separately. We simulate an averaged estimate signal Est_{av}, analogous to S_{av}, using the *a priori* values. The idea being that $Est_{av}(i_m)$ should follow the $S_{av}(i_m)$ variations relatively closely for all i_m measurements wherein no cloud nor ice are present, while for the measurements affected by the presence of clouds or ice, S_{av} would increase relatively to Est_{av}. Est_{av} is used to select the cloud- and ice-free (CIF) reference measurements (i.e. all the measurements for which S_{av} remains close or below to Est_{av}). These CIF measurements are then used to build a CIF averaged signal S_{av}^{ref} (and a CIF ratio $R_{l/s}^{ref}$) to which S_{av} ($R_{l/s}$) is then compared in order to determine if the cloud detection threshold t_{av} (resp. $t_{l/s}$) is exceeded. A cloud is thus detected when both conditions are verified:

$$\begin{cases} S_{av}(i_m) > (1 + t_{av}) S_{av}^{ref}(i_m) \\ R_{l/s}(i_m) > (1 + t_{l/s}) R_{l/s}^{ref}(i_m) \end{cases}$$

where S_{av}^{ref} ($R_{l/s}^{ref}$) is obtained from S_{av} ($R_{l/s}$) using a weighted average on the nearest CIF measurements (the weight depends on the spatial proximity and surface elevation).

The cloud detection method will be described in more detail in a next paper dedicated to the results of our cloud retrieval with SPICAM (in preparation). It includes a comparison with the results obtained by OMEGA, another spectrometer on board MEX.

2. Creation of the *a priori* atmosphere:
   The atmosphere is divided into 13 layers wherein we specify the characteristics and *a priori* quantities of each RT component. The thickness of the layers increases with altitude in order to partly compensate the decrease of density.
   The *a priori* atmosphere come from the MCD v5.0, generated by the General Circulation Model (GCM) developed at LMD (Laboratoire de Météorologie Dynamique, Paris, France) by Forget et al. (1999). The MCD provides the vertical profiles of temperature, pressure and mixing ratios for gases (O_3 and CO_2) and dust. A cloud layer, capping the dust layer (Smith et al., 2013), is added in the system if detected by the cloud detection routine (step 1). The parameters used to model the atmosphere are described in more detail in next Section 3.3.
   Here ends the preparation part and is followed by the iterative part consisting in repeating step 3 (RT calculation) and 4 (inversion) until convergence (step 5) is achieved (with a maximum of 8 iterations).
3. Radiative transfer calculation:
   To perform the RT calculation, we use LIDORT (Linearised Discrete Ordinate Radiative Transfer, Spurr et al. (2001); Spurr (2002); Spurr (2004)), a RT code based on the discrete ordinate method (Chandrasekhar, 1960). LIDORT can generate radiances in a plane-parallel multi-layer atmosphere. It includes a pseudo-spherical correction for the treatment of the solar beam attenuation and takes into account multiple scattering occurring in the atmosphere. The treatment of surface reflection is also included.
   The v3.3 of LIDORT was adapted to our needs. We use it to simulate the spectrum using the built atmosphere and the varying retrieval parameters. It also calculates the spectrum analytical derivatives

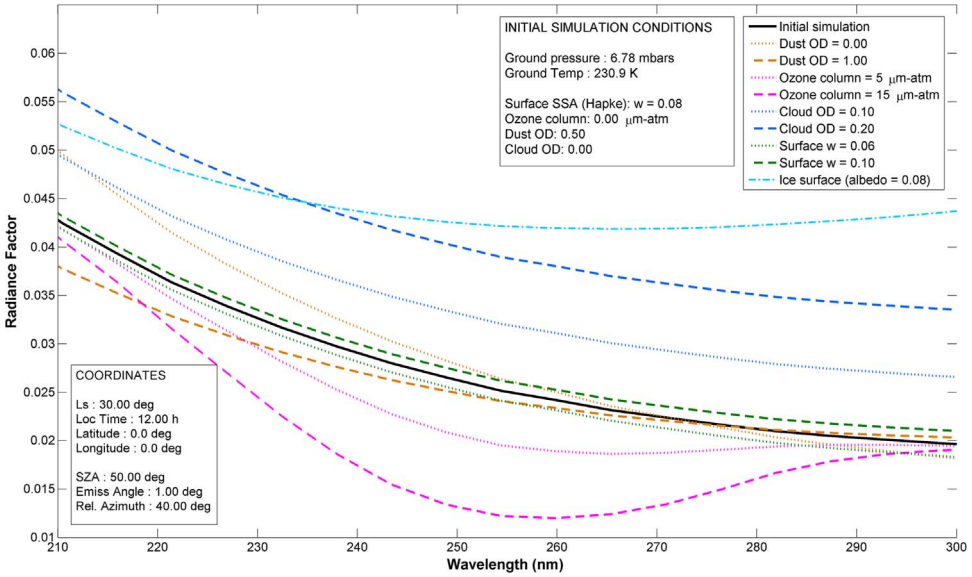

Fig. 5. Example of simulations showing the influence of the parameters.

associated to the retrieval parameters that are necessary for the inversion.

4. Inversion:
   We have implemented the optimal estimation method (OEM) of Rodgers (2000). It calculates a new set of values for the retrieval parameters in order to produce a new simulated spectrum (SS) that will converge toward the measured spectrum (MS).
   The new set of parameters' values is linearly extrapolated from the current set using: the analytical derivatives (calculated at step 3); the residue between the current SS and the MS (= SS-MS); the measurement error; and the *a priori* value of each parameter (for which we have to specify its variance to represent how much the parameter may vary around the *a priori* value). More details about the OEM implementation is given in Section 3.2.
5. Convergence test:
   This routine verifies if the retrieval procedure has converged. There are two possibilities of convergence. The first and ideal case is when the SS fits enough to the MS. To estimate the fit quality, we use a relative residue: (SS-MS)/DMS. DMS is the dataset mean spectrum which represents the average over all spectra of all orbits of whole the dataset. The convergence is reached when the root mean square (RMS) of the relative residue is minimised i.e. when it becomes lower than a defined convergence criterion ϵ. The RMS is calculated as:

$$\mathrm{RMS(SS-MS)} = \sqrt{\frac{1}{N_\lambda}\sum_{\lambda}\left(\frac{\mathrm{SS}(\lambda)-\mathrm{MS}(\lambda)}{\mathrm{DMS}(\lambda)}\right)^2} \tag{1}$$

   where N_λ and λ are respectively the number and index of spectral pixels considered. The convergence criterion is calculated as the RMS of a 2% fraction of the DMS ($\epsilon = 0.02$).
   The other convergence criterion is when all the parameters' values converge. It happens when the minimisation process reaches a minimum which implies that the residue and parameters only hardly vary between two consecutive iterations. We consider that the parameters have converged if they do not vary between two iterations by more than a defined fraction (0.5%) relative to a reference value which corresponds generally for each parameter to a typical low-to-moderate value (regolith SSA: 0.07, ice albedo: 0.03, O_3 column: 5 μm-atm, dust OD: 0.5 and cloud OD: 0.2; a description of the parameters is provided in Section 3.3).
6. Saving results:
   Once the convergence is achieved or after a maximum of 8 iteration loops, the procedure ends and saves the results. We keep the best set of parameters' values, i.e. the set that gave the smallest RMS during the iterative procedure.

3.2. Implementation of the optimal estimation

The inversion of the parameters' values from the observed spectra is performed using the optimal estimation method (Rodgers, 2000). The general equation of the radiative transfer forward model can be written as:

$$y = f(x, b) + \epsilon \tag{2}$$

where y is the measurement vector (the measured radiance factor in this case), x is the true state vector (the parameters to be retrieved i.e. the ozone column, the dust and cloud opacities and the surface albedo) and b represents the additional parameters used by the forward model function f. The forward function f describes the complete physics of the measurement, including the description of the instrument. In the case of a moderately non-linear problem, the best estimate $\hat{x}$ of the solution of Eq. (2) is found by solving iteratively the equation:

$$x_{i+1} = x_a + G_i[(y - f(x_i)) + K_i(x_i - x_a)] \tag{3}$$

where the subscripts i and $i+1$ refers to the iteration loop number, x_a is the *a priori* of the state vector (i.e. the best knowledge of the parameters), K_i is the jacobian matrix containing the derivatives of f relative to the parameters:

$$K_i = \frac{\partial f}{\partial x_i} \tag{4}$$

These derivatives are provided by the RT model. We can finally define the gain matrix G_i:

$$G_i = (S_a^{-1} + K_i^T \cdot S_\epsilon^{-1} \cdot K_i)^{-1} \cdot K_i^T \cdot S_\epsilon^{-1} \tag{5}$$

where S_ϵ is the error covariance matrix of the measurements and S_a is the *a priori* covariance matrix. S_ϵ is set to be diagonal and represents the error on the radiance factor as described in Section 2.4. S_a also is set to be diagonal and represents the *a priori* parameters' variance, i.e. one scalar for each parameter.

Inversion error. The error on the retrieved parameters is obtained from two contributions: the smoothing error (S_{smoo}), which accounts for the sensitivity of the measurements/forward model to the variable to be retrieved (i.e. the measurement/forward model system does not allow perfectly reproducing the true atmosphere, but a smoothed value of it), and the error due to the measurement noise (S_{meas}). They can be expressed as:

$$S_{smoo} = (A - I) \cdot S_a \cdot (A - I)^{-1} \tag{6}$$

$$S_{meas} = G \cdot S_\epsilon \cdot G^T \tag{7}$$

where I is the identity matrix and A the averaging kernel matrix defined by:

$$A = \frac{\partial \hat{x}}{\partial x} = \frac{\partial \hat{x}}{\partial y}\frac{\partial y}{\partial x} = G \cdot K \tag{8}$$

We did not consider here the forward model error due to the additional parameters b and the error on the forward model itself. In that case, the total covariance error is given by the matrix $S = S_{smoo} + S_{meas}$ and can be rewritten as:

$$S = (S_a^{-1} + K_i^T \cdot S_\epsilon^{-1} \cdot K_i)^{-1} \tag{9}$$

Degree of freedom. As shown by Eq. (8), the averaging kernel matrix A represents the sensitivity of the retrieved parameters to the true parameters. We use the diagonal terms (A_{ii}) to obtain informations whether the retrieved values of the parameters are extracted from the measurement or are rather coming from the *a priori*. These A_{ii} terms vary between 0 and 1 (as we consider only integrated columns) and are called degree of freedom (DoF): a DoF of 1 indicates that the retrieved value of the parameter was entirely deduced from the measurement while a DoF of 0 means that the retrieval was not sensitive in this parameter and the retrieved value comes therefore from the *a priori*. In the present case, there is one A_{ii} corresponding to each parameter (thus 4 in total for: ozone, dust, cloud and surface reflectance).

3.3. Atmosphere parametrisation

We describe here the parameters used to model the interactions of the UV radiation with the atmosphere: the absorption by ozone molecules, the molecular "Rayleigh" scattering and the absorption and scattering induced by aerosols (dust and ice clouds). The influence of the different parameters on a R_f spectrum is shown in Fig. 5.

3.3.1. Ozone absorption

In the 220–290 nm range, the radiation is absorbed by Hartley band of ozone. That band is centred around 255 nm where absorption is the strongest. In this work, we have considered the recent cross-sections from the dataset of Gorshelev et al. (2014) and Serdyuchenko et al. (2014), which are in agreement with the results of the other previous works on ozone absorption of Brion et al. (1993) and Malicet et al. (1995). The uncertainty on the measurements is estimated to be within 2–3%.

The dataset contains eleven cross-sections measured at different temperatures extending from 193 K to 293 K by step of 10 K. However, the influence of temperature on the Hartley band is much weaker than in other spectral regions as explained in Serdyuchenko et al. (2014). As the temperatures at which ozone is retrieved usually vary between 150 K and 290 K, it implies that the difference with the cross-section temperature should not exceed 50 K. In our case, we estimate that the error on the cross-section due to appropriate temperature should therefore remain below 1% (based on Serdyuchenko et al. (2014)).

3.3.2. Rayleigh scattering

Rayleigh scattering is induced by the molecules in the atmosphere. The Rayleigh cross-section and phase function (PF) used in this work were calculated from several previous works considering an atmosphere made of 96% CO_2, 2% N_2 and 2% Ar.

The final Rayleigh cross-section was therefore obtained as follow: $\sigma = 0.96\sigma_{CO2} + 0.02\sigma_{N2} + 0.02\sigma_{Ar}$. For N_2 and Ar, we used the theoretical cross-sections calculated as in Sneep and Ubachs (2005) which both shows a very good agreement with their measurements (<1%, they worked between 470 and 570 nm). For CO_2, as theory and measurements in Sneep and Ubachs (2005) do not show such a good agreement, the cross-section was derived using a fit on the measurements in the UV from Shemansky (1972), Karaiskou et al. (2004)[1] and Ityaksov et al. (2008). Due to the wavelength dependence of the refractive index and the King factor, the expression giving the Rayleigh cross-section is not exactly proportional to the $1/\lambda^4$ law (where λ is the radiation wavelength) and can be written as proposed in Ityaksov et al. (2008): $\sigma_R = \overline{\sigma}\nu^{4+\epsilon}$, where ν is the light wavenumber in cm^{-1}. The parameters $\overline{\sigma}$ and ϵ were deduced by a linear fit by taking the logarithm of the equation to obtain the following values: $\overline{\sigma} = 2.247 \times 10^{-45}$ and $\epsilon = 0.3801$.

The Rayleigh phase function $p(\cos\theta)$, where θ is the scattering angle, is decomposed in Legendre polynomials and requires two components: the zero order which coefficient is always equal to unity ($\beta_0 = 1$) and the second order which coefficient is related to the depolarisation ratio δ ($\beta_2 = \frac{1-\delta}{2+\delta}$). The depolarisation ratio used was obtained using the individual depolarisation ratios of the three gases considered CO_2, N_2 and Ar. For N_2 and Ar, they were calculated as in Sneep and Ubachs (2005) and for CO_2 it was taken from Karaiskou et al. (2004). The final depolarisation ratio used to calculate the PF is $\delta \approx 0.0777$. The obtained Rayleigh scattering PF is shown in green in Fig. 6.

3.3.3. Dust

Dust aerosols are responsible for absorbing and scattering the UV radiation. We consider the total vertical optical depth (OD) τ_d to quantify their extinction and the single scattering albedo (SSA) $\widetilde{\omega}_0$ to represent the scattered fraction. In this work, we use the dust properties of Wolff et al. (2010). For the SSA, we consider $\widetilde{\omega}_0 = 0.622$ at 258 nm and $\widetilde{\omega}_0 = 0.648$ at 320 nm. The PFs come from T-matrix calculation (Mishchenko et al., 1996) using a 1.5 μm cylindrical-shaped particles (Wolff et al., 2009) that was modified to agree with measurements as described in (Wolff et al., 2010): MRO/MARCI's EPF measurements were used to constrain and optimise the side-scattering (around 260 and 320 nm), while the back-scattering part was modified using the ground-based measurements from the Imager for Mars Pathfinder of Tomasko et al. (1999) at 444 nm. These PFs are shown in Fig. 6 and produce a predominantly forward scattering.

The SSA and PF used for the 220–290 nm interval in the present work were obtained by linear extrapolation of the 260 and 320 nm references.

3.3.4. Clouds

Water ice absorption coefficient is very weak in the spectral region between 200 and 390 nm (Warren and Brandt, 2008). Ice cloud absorption is therefore negligible and the single scattering albedo is set equal to unity $\widetilde{\omega}_0 = 1$. The cloud opacity τ_c is thus entirely due to scattering. No wavelength dependence of the SSA is considered.

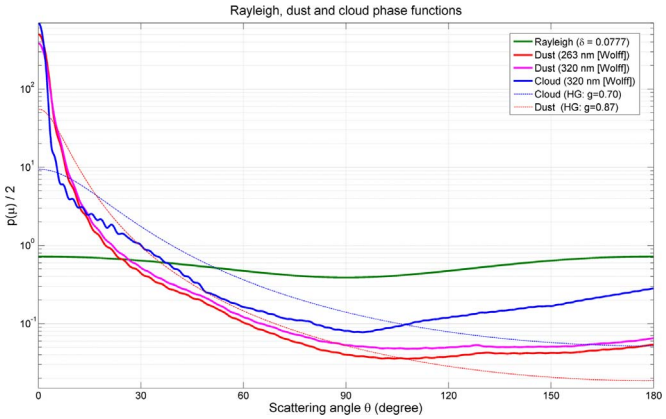

Fig. 6. Phase functions of the different scattering processes considered in this work ($\mu = \cos\theta$). The Rayleigh scattering that occurs on atmospheric molecules is approximately isotropic (using a depolarisation ratio of 0.0777). The Mie scattering induced by larger dust and ice cloud particle is directed forward. However, clouds present a noticeable more important back-scattering probability than dust. For comparison, the dashed lines represent the Henyey-Greenstein (HG) phase functions with asymmetry parameter g = 0.87 and g = 0.70 as used in Mateshvili et al. (2007a), (2007b). (For interpretation of the references to color in this figure legend, the reader is referred to the web version of this article.)

The PF used for ice clouds was provided by M.J. Wolff (personal communication, Wolff et al., in preparation). They used 3 μm ice particles size with a droxtal shape (Yang et al., 2003). No wavelength dependence was considered for the cloud phase function, which is shown on Fig. 6.

3.4. Surface parametrisation

3.4.1. Regolith surface

To model the reflection of light on the Martian surface, we use the bidirectional reflectance of Hapke's theory (Hapke, 2005). We implemented the scenario case of the reflectance over large scale area of a rough surface. This formalism takes into account the opposition effect which induces a enhancement of back-scattering in the opposite direction to incident light.

The Hapke parametrisation used in this work for regolith surface comes from Wolff et al. (2014), which is in the continuity of the previous works of Wolff et al. (2009) and Wolff et al. (2010) that used EPF (emission phase function) observations from respectively CRISM and MARCI on board MRO to derive the surface parameters (Hapke parameters were estimated for large areas in low dust loading conditions). The SSA ω_0 used as *a priori* is location and wavelength dependent (extrapolated from Wolff et al. (2014), results) and varies between 0.05 and 0.11 (300 nm). The other parameters are kept constant: the opposition effect magnitude $B_0 = 1.0$; the opposition effect width $h = 0.06$; the asymmetry parameter $b = 0.27$, the forward scattering fraction $c = 0.30$ and the macroscopic roughness $\overline{\theta} = 20°$.

3.4.2. Ice surface

The values of Lambertian albedo used to represent the reflection on ice polar caps were taken from James et al. (2005) which studied the southern polar cap with the High Resolution Camera on Hubble Space Telescope. They deduced values of the polar cap albedo from the visible down to the UV range.[2]

[1] The value at 206nm was not taken into account in the fit.

[2] We have selected the results obtained for "point 1" in James et al. (2005) which is considered as the more reliable due to known dust conditions measured nearby by MGS TES. We considered the average value of the three measurements at L_s= 235°, 251° and 265°.

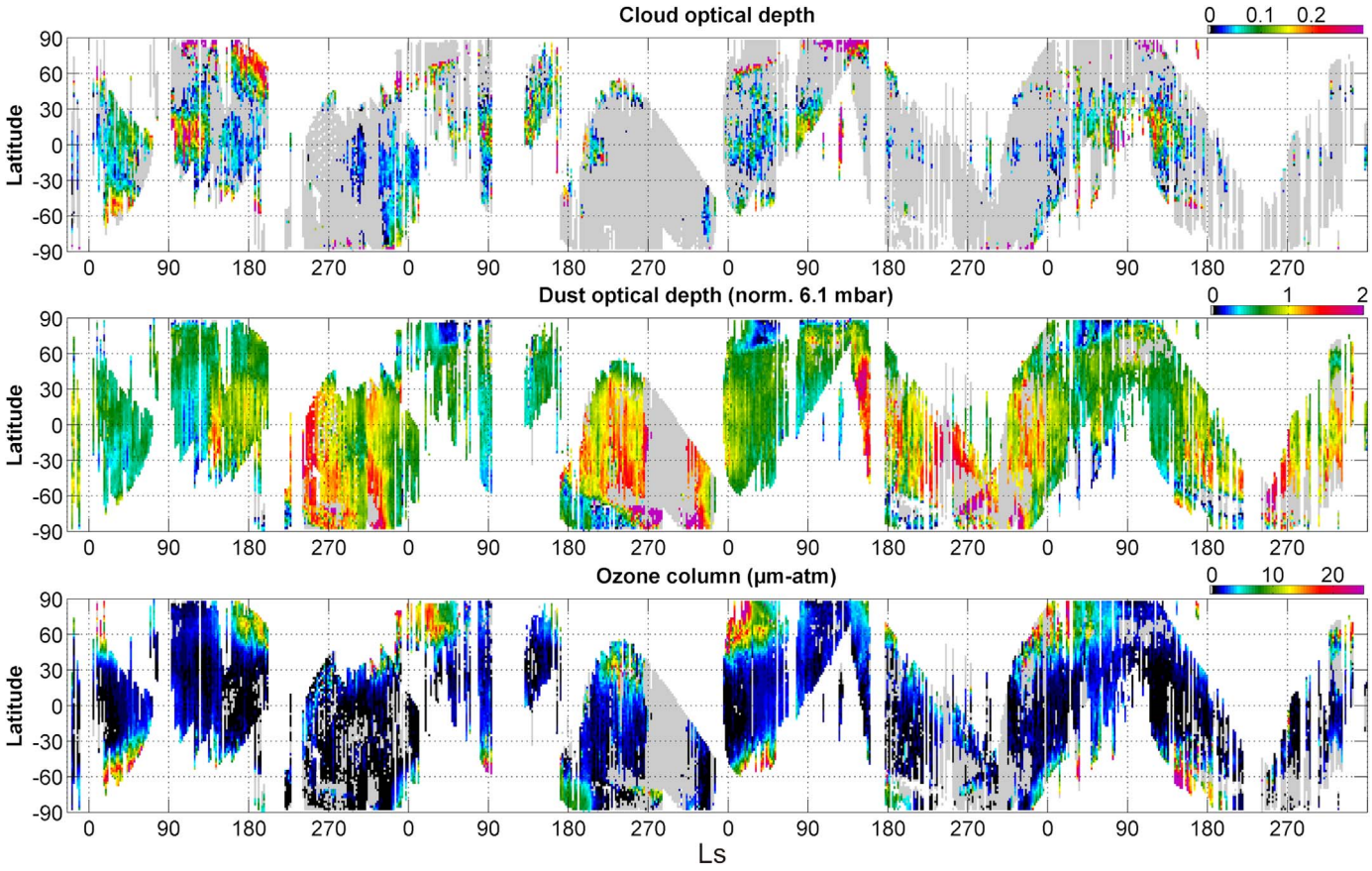

Fig. 7. Seasonal evolution of the zonally averaged cloud opacity (top), dust opacity (middle, normalised at 6.1 mbar) and ozone column in μm-atm (bottom). The map covers the period going from late MY26 to the end of MY30, using a 2° × 2° grid. The white areas correspond to regions where no measurements were performed, the grey background represents the measurement coverage and the colour scale ranging from black to purple indicates the retrieved quantities.

These results were obtained for a relatively high albedo region located on the seasonal polar cap made of CO_2 ice (dry ice). Some deviations due to composition in the seasonal northern cap are possible, as well as seasonal variations and inter-annual variability (e.g. Hale et al., 2005; Langevin et al., 2007; Byrne et al., 2008) and also lowering of the reflectivity due to dust settling (e.g. Kieffer, 1990; Hansen, 1999)). As *a priori*, we considered an albedo value of 0.20 at 330 nm, a compromise between the values in James et al. (2005) and the dark dust albedo. The wavelength dependence was obtained by a linear extrapolation of the values at 250 and 330 nm from James et al. (2005).

4. Examples of output climatologies

In this section, we show and discuss the climatologies obtained with the retrieval model using the nadir SPICAM/UV measurements of more than 4 Martian years (from MY 26.9 to 31.0). To produce these climatologies we used an exclusion criterion on the degree of freedom (DoF) of each parameter. Only retrieved parameters with a DoF >0.4 were kept to ensure that the retrieved value does not come only from the *a priori*. Another selection criterion is used on the retrieval residue to include only the retrievals that have a RMS < 0.04.[3] The seasonal distributions of the 3 retrieved atmospheric species, i.e. cloud OD, dust OD and ozone, are shown in Fig. 7.

[3] The maps provided in the following were obtained by satisfying the criterion for (at least) one of the two RMS calculations given hereafter: the RMS as described in Eq. (1) of Section 3.1; and a modified RMS where the "DMS" (data mean spectrum) of Eq. (1) is replaced by the measured spectrum (MS). This modified RMS was set as we remarked that the criterion on only the first RMS was sometimes to restrictive for high signal measurements by rejecting some fit that we consider acceptable.

4.1. Clouds

4.1.1. Climatology overview

The top panel of Fig. 7 represents the seasonal evolution of the cloudiness. The two principal cloud features, the aphelion cloud belt (ACB) and the polar hoods, are both clearly observed. These water ice clouds are known to be repeatable from year to year (Smith, 2004, 2008). The results of the 4 MY analysis are combined in Fig. 8 for a more visual overview of these cloud features.

The ACB occurs every year at low latitudes during the aphelion season (Smith, 2004, 2009). Its different stages are well visible in Fig. 8: the formation starts around $L_s = 20 - 30°$, it shows a maximum extension and intensity between $L_s = 80°$ and $L_s = 140°$ and quickly disappears after. At its maximum of activity, the ACB completely encircles the planet at the Equator as shown in Fig. 9 top left. Around perihelion, (almost) no equatorial clouds are observed (cf. Fig. 9 top right), except over Arsia Mons (clouds over volcanoes is discussed further). From the inter-annual point of view, we can see parts of the ACB stages in each MY in Fig. 7 top, depending on the coverage. The main changes from one year to the other are generally related to dust storms: As for example in MY27 where the cloud belt stops abruptly earlier in the season than usual (around L_s=135°) due to the rise of a local dust storm event (cf. Fig. 7 middle), and which was also observed by THEMIS (Smith, 2009).

The polar hoods is known to occur above the polar regions of the winter hemisphere (Benson et al., 2010, 2011). Parts of their edges can be seen in Fig. 7. The start of the northern polar hood (NPH) is well visible between $L_s = 160°$ and $L_s = 200°$ of MY27. We can see from the bottom panel of Fig. 9 that the hood covers all longitudes, in agreement

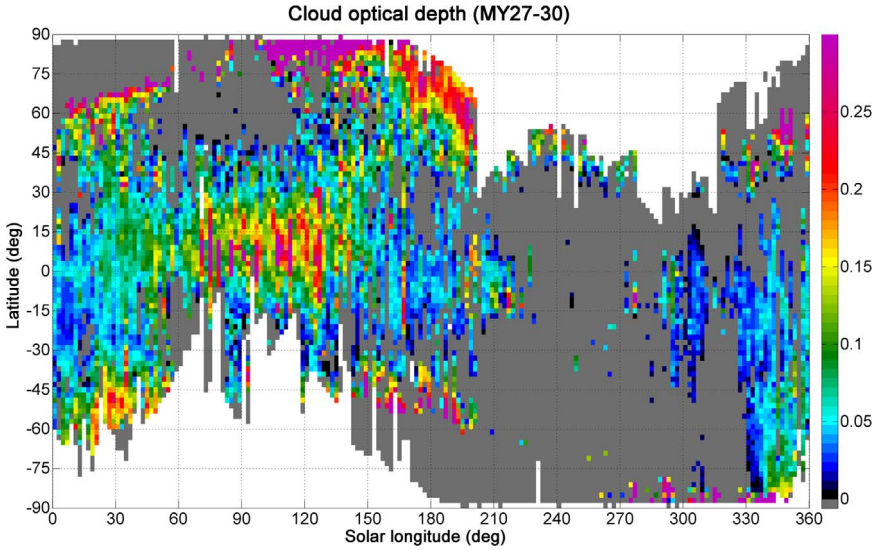

Fig. 8. Seasonal evolution of the zonally averaged cloud opacity. The values are averaged on the four Martian years of the dataset (from MY: 26.9 to 31.0).

with MRO/MCS (Benson et al., 2011) which showed that NPH was forming a cloud cap above the pole. The edge of the NPH has also been observed around L_s = 240° during MY28 and between L_s=330–350° in MYs 27 and 29. The southern polar hood (SPH) is also observed: Parts of the SPH edges are observed in the four MYs between L_s=0–60° (identified as SPH "phase 1" in Benson et al. (2010)) and between L_s=120–200° during the MYs 27 and 29 (identified as SPH "phase 2" in Benson et al. (2010)).

The tall volcanoes are particularly favourable for cloud formation. Orographic clouds form because of adiabatic cooling that occurs with upslope winds arising on these volcanoes (Hartmann (1978)). Ice clouds are often observed above or near these volcanoes (Benson et al., 2003, 2006), with some example visible in Fig. 9: On the top left panel, we observe that the highest retrieved opacities observed during the ACB maximum activity, are located over the large elevated Tharsis plateau, Olympus Mons [18 °S – 134 °W] and Elysium Mons [25°S–147°E]; On the top right panel, we notice that the only cloud retrieved around perihelion is located above Arsia Mons [10°S–120°W]

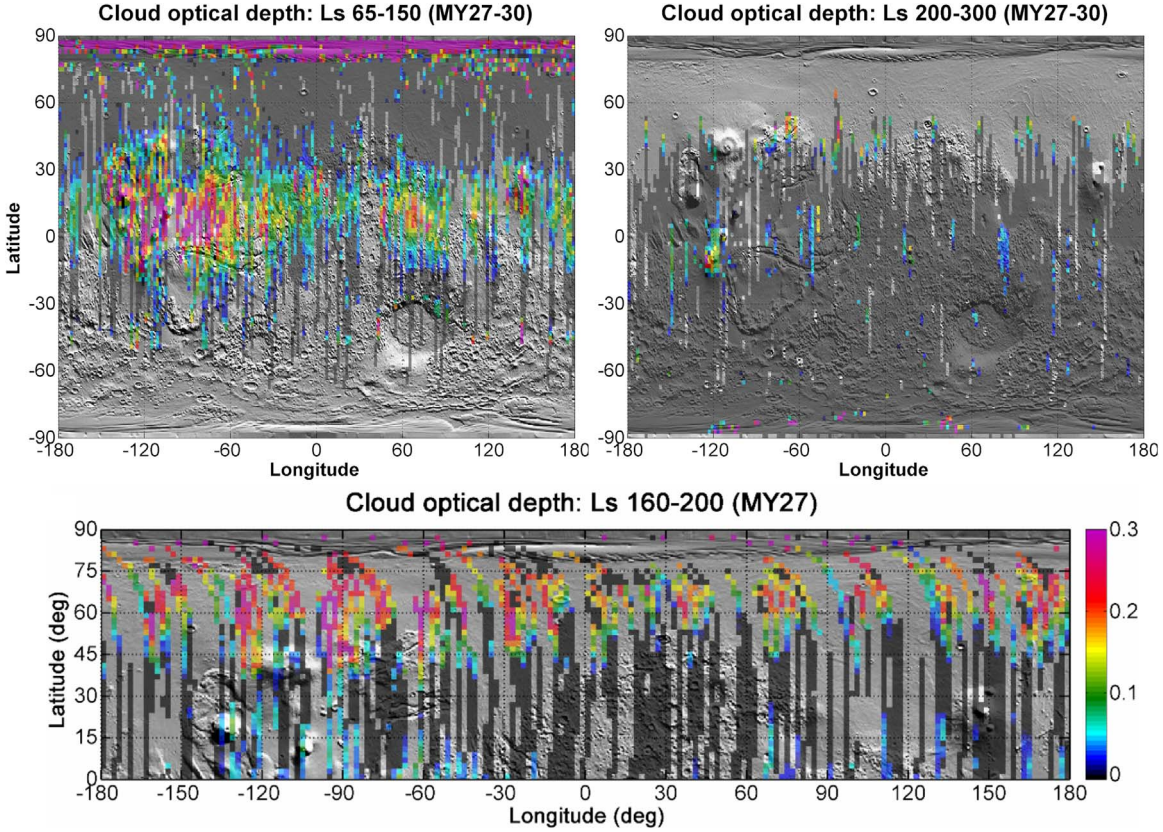

Fig. 9. Example of spatial distribution of cloud OD for tree different periods. On the top left panel, period L_s = 65 – 150° (MY27-30), the ACB is clearly visible encircling the whole planet at low latitude. The top right panel, period L_s = 200 – 300° (MY27-30), corresponds to the cloud free season where (almost) no cloud were retrieved except above Arsia Mons [10°S–120°W]. The bottom panel highlights the NPH observed between L_s = 160 – 200° of MY27. The maps are averaged on a 2° × 2° grid using the same colour scale. Darkened pixels indicates the measurement coverage and the colour scale ranging from black to red corresponds the retrieved cloud opacity.

Table 1
Summary of the inversion error on cloud OD retrieval.

Conditions	Error
$\tau_c \sim 0.05$	15–20%
$\tau_c \sim 0.1 - 0.2$	~10%
$\tau_c \geq 0.3$	~5%

which is known to be covered by clouds for the major part of the year (Benson et al., 2006).

A detailed analysis is left for a future paper (in preparation) dedicated to our ice cloud retrievals. The paper will provide comparisons with results from other works using: MGS/TES (Smith, 2004), Mars Odyssey/THEMIS (Smith, 2009), MEX/SPICAM (Mateshvili et al., 2009) and MEX/OMEGA (Madeleine et al., 2012) concerning equatorial clouds; MRO/MCS (Benson et al., 2010, 2011) for the polar hoods; MGS/MOC (Benson et al., 2003, 2006) for the cloud presence above volcanoes.

4.1.2. Degree of freedom, error and uncertainty

The DoF for the retrieved cloud optical depth (COD) is larger than 0.9, implying that the retrieved values come from the measurements. The retrieval error on COD τ_c lies generally between $\sigma_c = 0.005 - 0.025$, increasing with cloud thickness. The relative error decreases as clouds are thicker and is summarised in Table 1.

However, this error does not include the uncertainty associated to the assumptions such as the cloud altitude or the scattering PF for which we have performed sensitivity studies on 7 orbits. It shows that the cloud PF has a strong influence on the retrieved COD. We compared the results obtained with the PF used in previous SPICAM/UV works of Mateshvili et al. (2007b), Mateshvili et al. (2009) (using the value g = 0.70) to these obtained with the nominal PF, both represented in Fig. 6). Fig. 10 shows COD variations up to 400% and the different colours emphasise that the variations strongly depend on the phase angle: variations are the largest at low phase angle, decrease as the phase angle increases and become negative for phase angle >70°. Such a trend is expected when comparing the back-scattering tail of the PFs. From the convergence point of view, we observe only a little impact on the RMS (generally ΔRMS < ± 0.001).

The influence of the cloud altitude appeared to be less important. We tested low altitude cloud around 10–15 km (typical for ACB Smith et al. (2013) and used nominally in this work) compared to more elevated clouds (35 km, typical for polar hoods Benson et al. (2010), Benson et al. (2011)): Fig. 11 shows that the COD decreases between 0–4% when SZA is not too high (<65°). For these cases, a minor impact on the RMS is observed (ΔRMS < ± 0.001). Several higher COD variations (5–70%) are observed and correspond to cases with higher SZAs (>65°). These cases are also characterised by less good convergence of the fit with a decrease of the RMS (ΔRMS >0.005). The impact of the altitude of clouds seems therefore limited at low and mid SZA but can become important at high SZA, which has probably an impact on the polar hoods.

4.2. Dust

4.2.1. Climatology overview

The middle panel of Fig. 7 represents the seasonal evolution of the dust opacity. We notice first that the expected dust loading difference between “clear” aphelion season and “dusty” perihelion season is clearly visible (e.g. Smith, 2004, 2009): the dust OD being lower and relatively constant around aphelion while it is larger and more variable during perihelion. This can also be seen in Montabone et al. (2015), hereafter abbreviated “MON15”, that used assimilation of the TES, THEMIS and MCS data to produce dust climatology between MY24-31. A second noticeable detail is the presence of important gaps during the perihelion season that actually correspond to dust storm events and for which our retrievals have not converged (this will be discussed further in the text).

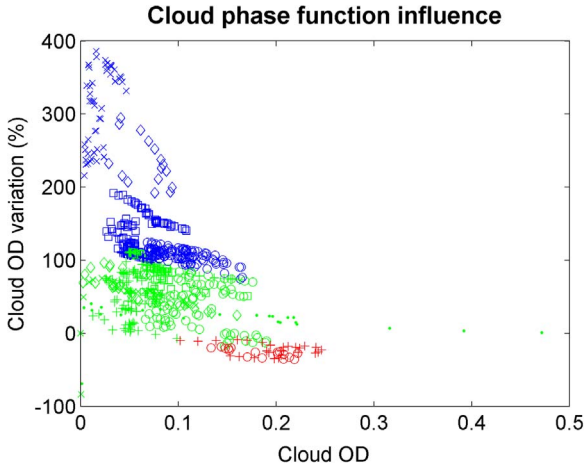

Fig. 10. Influence of the cloud phase function on the retrieved cloud opacity. The “y” axis shows the variation of retrieved COD when using the PF defined in Mateshvili et al. (2007b), Mateshvili et al. (2009) (g = 0.7) instead of the nominal PF. The “x” axis represents the retrieved COD (nominal). The different markers represent the orbits: 232 (crosses, L_s = 9°), 331 (squares, L_s = 24°), 380 (circles, L_s = 31°), 424 (+, L_s = 36°), 891 (dots, L_s = 94°), 1385 (diamonds, L_s = 160°) and 1479 (triangles, L_s = 174°). The colours represent the phase angle range: phase ≤ 35° in blue, 35°< phase ≤ 70° in green and phase >70° in red. (For interpretation of the references to color in this figure legend, the reader is referred to the web version of this article.)

During aphelion, we can clearly distinguish the low dust OD patterns associated to the presence of the aphelion cloud belt, highlighting the anti-correlation between dust and clouds: the dust optical depth reaches a minimum when the ACB is present at low latitudes between L_s=70–140°. Outside the ACB and the polar caps, the dust opacity is relatively constant before L_s=140°. Yet, some exceptions of higher opacities are observed: Several yellow spots are found at high latitudes in the northern hemisphere, especially during MY 29 and 30 after L_s=90°, which are probably due to local dust storms that are likely to occur in the vicinity of the polar cap (Cantor et al., 2001). Another DOD increase is observed at low latitude around L_s=55° of MY 30, it is possibly related to a storm located on the Tharsis bulge between [110–70°W], but is not confirmed by MON15. Another exception that worth to be highlighted is the dust increase around L_s=135° at low latitudes in MY27. The cause of this increase is a dust storm that arose a little earlier than usual in the aphelion season. This storm was also observed by THEMIS (Smith, 2009) and by both MERs (Smith et al., 2006). This was already mentioned in the cloud section as it is the reason for the early disappearance of the ACB. Another special case is the strong increase observed between L_s= 145-155° of MY29 around 30°N. An increase of the dust activity is also visible in MON15 below mid latitudes at that corresponding period. The MER Spirit also recorded a very narrow but intense peak around L_s=155° (visible in the upper plot Fig. 13), which is also captured by our retrievals: SPICAM measurements near[4] the Spirit site reveal indeed usual opacity at L_s= 147° followed by a strong increase at L_s=153° and a return to nominal level at L_s= 157°.

During perihelion, the dust loading significantly increases and is known to have an important inter-annual variability due to dust storm activity (Smith, 2004, 2009). We observe this variability when comparing the patterns in the 4 MYs, as for example with the appearance of the first storm: it appear around L_s=135° for MY27 while and around L_s=155° for MY30. For MY28 and 29, the measurement coverage is not optimal between L_s=140°-180°, but storm are observed from around L_s=

[4] The measurements were obtained at the same latitude and within ± 11° of longitude.

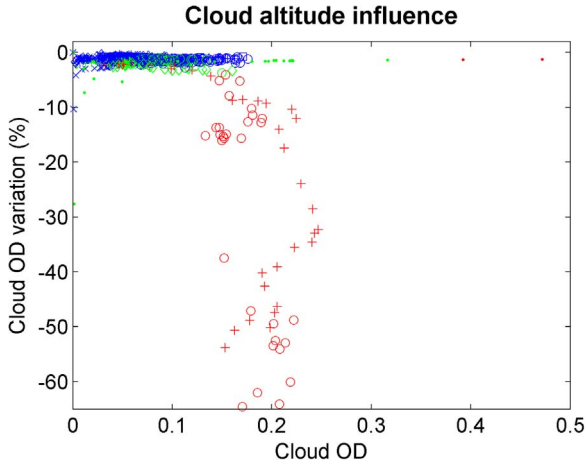

Fig. 11. Influence of the cloud altitude on the retrieved cloud opacity. The "y" axis shows the variation of retrieved COD when using an elevated cloud layer (35 km) instead of the nominal cloud altitude (~10–15 km), using in both cases layers of 5 km thickness. The "x" axis represents the retrieved COD (nominal). The different markers represent the orbits (cf. Fig. 10). The colours represent the SZA range: SZA ≤ 50° in blue, 50°< SZA ≤ 65° in green and SZA >65° in red. (For interpretation of the references to color in this figure legend, the reader is referred to the web version of this article.)

170° and L_s=145° respectively. The coordinates (L_s, Lat) of the first storms for the four MYs match well with those of MON15 climatology.

As mentioned, we observe gaps during the perihelion season which correspond to the important increases of the dust loading due to the large storm events: for example, we observe a large gap in MY28 between L_s=270–320° when a thick dust layer was present in the atmosphere due to the global dust storm that occurred that year. These gaps are explained by the fact that our retrieval does not converge when the dust OD becomes very large. From Fig. 5, we can see that the presence of dust results in a decrease of the R_f. And as we will show later, our retrieval finds larger DOD than other results in the UV–visible, which could reflect possible shortcomings in the dust modelling (e.g. optical properties, altitude distribution). Our retrieval procedure seems to compensate this impact by using more dust than really present in order to lower the simulated spectrum and to match the measured one. When the dust loading becomes very large, the measured spectrum becomes very low and can not be fitted by the simulated spectrum. The reason for this could be that above a certain thickness of the dust layer, the opacity has (almost) no more influence on the R_f. The simulated spectrum approaches the measured spectrum but is unable to lower enough to reach it, no matter how much dust is set. So actually, in these cases, very high dust ODs are retrieved by the inversion procedure which however never converges resulting in much larger RMS values. The "edges" of these storm events are visible and their retrieved opacities are often relatively large, suggesting a rise of dust OD. Fig. 12 shows the dust climatology obtained when the convergence criterion that has been significantly relaxed, revealing the large DOD increases that can be used for an easier qualitative comparison with MON15. The comparison reveals a general qualitative agreement between the two datasets and the coordinates of the major storms match well.

Our results for dust OD show a qualitative agreement with previous works. However, the retrieved DODs are usually higher when comparing to other studies in the UV–visible such as the MER/Pancam results (Lemmon et al., 2015) or the results obtained by MRO/CRISM (from private communication with M.J. Wolff, related to Wolff et al. (2009)). Fig. 13 shows the comparison with the results of Lemmon et al. (2015) using the MER/Pancams: We notice that the SPICAM OD are always higher than those obtained from Spirit. The agreement is better with Opportunity for which the retrieved ODs sometimes similar, and always higher for the rest. It is however important to precise that the MER results give the total aerosol opacities (ice cloud + dust) while those of SPICAM are given separately (magenta and green markers) and should therefore be summed when clouds are present for an adequate comparison.

Different possible reasons could explain this discrepancy. 1) The altitude profile: we use modelled profiles from the MCD v5.0 (Madeleine et al., 2011) which differ from the profiles measured by MRO/MCS (Kleinböhl et al., 2009). MCS observes a maximum in altitude which is not reproduced in MCD profiles (Navarro et al., 2014). And as shown in Fig. 14, an increase of the dust elevation results in a decrease of the retrieved DOD and also improves the convergence (i.e. lower the RMS) in the large opacity cases. This shows the altitude profile is therefore probably part of the solution; 2) the optical properties are derived from a unique particle size: the dust particle size is known to vary with season and with altitude (1–2.5 μm Clancy et al. (2003)); These explanations are being investigated and will be improved in future versions of our retrieval routine.

An example of spatial distributions is given in Fig. 15. It shows the expected anti-correlation between the retrieved dust OD and topography: higher optical depth are observed in the lowlands of the northern hemisphere, while the southern highland lies under a thinner dust aerosol layer. The deep Valles Marineris canyon and Hellas basin, where the dust ODs are higher, are also well contrasted with their surrounding highlands. While the minima in dust loading are well observed above the highest volcanoes (i.e. the three Tharsis volcanoes, Olympus Mons, Alba Patera and Elysium Mons).

4.2.2. *Degree of freedom, error and uncertainty*

The DoF for the dust OD (DOD) is larger than 0.8 when no clouds are present meaning that the retrieved values come from the measurement. It remains generally between 0.6 and 0.8 when clouds are present, indicating still a good sensitivity of DOD for these cases. The inversion error on the retrieved DODs varies generally between 10% and 40%, it decreases with increasing DOD and increases when clouds are present. The retrieval error is summarised in Table 2.

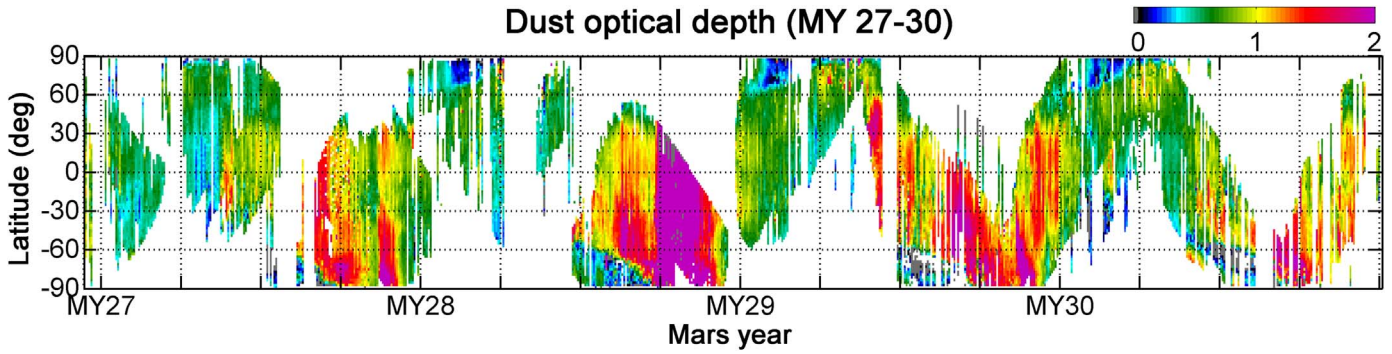

Fig. 12. Seasonal evolution of the zonally averaged dust opacity. This map must not be considered as reliable as the RMS criterion used to produce it was largely relaxed (RMS ¡ 0.2) but is useful to give a qualitative intuition of the large dust loading events.

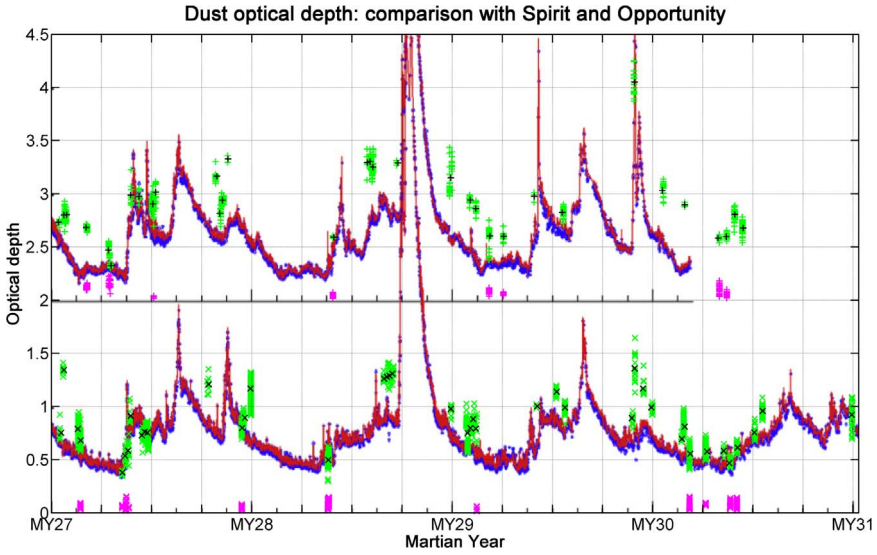

Fig. 13. Dust opacity (300 nm) retrieved by our method compared to the values obtained with the Pancam instrument on board Spirit and Opportunity rovers. The Pancams provide measurement of aerosol optical depth at 440 nm (dark blue dots) and 880 nm (red line) through direct solar imaging. Spirit measurements are offset by 2. SPICAM results are those obtained in a 6° × 6° box centred on each rover's location and are given by "x" (for Opportunity's site) and "+" markers (for Spirit's site, offset by 2). The dust and cloud optical depth are represented in green and magenta respectively. The dust OD average on $\Delta L_s = 5°$ intervals are also given (black symbols). It is useful to precise that the dust opacities at 300 and 440 nm are more or less similar (according to T-Matrix calculation, the OD at 300 nm is about 2–3% lower than at 440 nm). The Pancam opacity plots are reproduced from Lemmon et al. (2015). (For interpretation of the references to color in this figure legend, the reader is referred to the web version of this article.)

This error does not include the uncertainty associated to the assumptions i.e. the altitude distribution, the SSA or the PF for which we have performed some sensitivity studies. The influence of the altitude distribution was already highlighted in the case of the MY28 dust storm (cf. Fig. 14). We have also tested the impact of the use of a Conrath profile (Conrath, 1975) with parameter $\gamma = 0.03$ during the aphelion season (on the same seven orbits as in Fig. 10). The Conrath profile goes higher than the MCD average profiles used nominally in this work. It induces a decrease of the retrieved DOD generally between 30% and 55% that has little impact on the convergence ($|\Delta RMS| < \pm 0.001$) but is however usually slightly better with the more elevated profile. Larger DOD variations (up to −80%) are yet observed when relatively thick clouds ($\tau_c \geq 0.1$) or ice surface are present and SZA is large (>60°). In these cases, the impact on the convergence is important with $|\Delta RMS| > \pm 0.005$ for the largest DOD relative difference (but not particularly in favour of one of the two profiles). It shows that the altitude distribution has a significant influence on the retrieved DOD which decreases as the profile reaches higher altitudes.

The impact of the scattering properties were also tested, a sensitivity test was performed for two sets of SSA (ω_0) taken from Wolff et al. (2010): we compared the nominal values used for the retrieval $\omega_0 = 0.622 - 0.648$ to the values $\omega_0 = 0.630 - 0.653$ (258–320 nm) which corresponds to a 1.8 μm particle size. The test was performed for two periods: the period of MY28 dust storm and during MY27 aphelion period (same seven orbits as in Fig. 10). For the storm period, the use of the second SSA set induces a 2–3% decrease on the retrieved DOD compared to the nominal one. While for the aphelion period, we observe usually a 1–6% increase of the retrieved DOD that seems influenced by the cloud presence: generally 2–4% with clouds and 3–6% without (see Fig. 16). The impact on the convergence remains limited with a $|\Delta RMS| < \pm 0.001$. The studies of Wolff et al. (2010) shows a good agreement about the derived SSA with other works in the UV (e.g. Mateshvili et al., 2007a) and the error on ω_0 is estimated to be 0.022 at maximum. This suggests that the SSA is relatively well constrained implying that the uncertainty on the SSA should therefore have a relatively limited influence on the retrieved DOD.

The phase function has been also tested. We compared the retrieval results obtained with the dust PF used in previous works of Mateshvili et al. (2007a) to these obtained with the nominal PF (both PFs are represented in Fig. 6): Fig. 17 shows variations between [−10%, +80%] with the maximum decreasing from +80% at low DOD to +20% for the highest DODs. No clear trend related to phase angle is reported for the dust PF test (as it was the case for the cloud PF tests, cf. Fig. 10). This reflects the fact that the direct back-scattering due to dust is less important than it is with clouds, as it can be seen in Fig. 6. However, the presence of clouds or ice surface seems to influence the DOD variations as illustrates Fig. 17: the presence of cloud or ice is generally related to a larger variation than when none of them is present. The PF influences the retrieval convergence. The impact is generally limited with $|\Delta RMS| < \pm 0.001$ at low DOD ($\tau_d < 0.3$); Important RMS difference ($|\Delta RMS| > 0.004$) are frequently observed at high DOD ($\tau_d > 1.1$); Between $\tau_d = 0.3 - 1.1$, limited impact is observed except for the cloudy cases ($|\Delta RMS| = 0.002 - 0.007$) and for the cases of negative variations ($|\Delta RMS| = 0.001 - 0.003$).

4.3. Ozone

4.3.1. Climatology overview

The bottom panel of Fig. 7 represents the seasonal evolution of the ozone total column. We notice that the expected seasonal trend of ozone, anti-correlated to water vapour (e.g. (Fedorova et al., 2006; Lefèvre et al., 2004)), is well observed: the largest ozone quantities are observed at high latitudes in the winter hemisphere where water vapour has condensed on the polar cap. While the ozone columns are much lower at low latitudes and in the summer hemisphere.

The winter poles are not probed by SPICAM/UV due to the absence of solar illumination during the polar night, but the increase of ozone column at the edge of the winter polar region is clearly visible. During the spring in the northern hemisphere, the SPICAM measurements extend almost up to the pole which allows to observe there the decay of the polar ozone. The retrieved column in this high abundance region generally ranges between 5 and 25 μm-atm.

Outside the winter polar regions, i.e. at low latitude and in the summer hemisphere, we observe low columns of ozone, remaining generally below 3 μm-atm. However, we notice two relatively significant exceptions to this during the perihelion season ($L_s = 180 - 360°$) of MY28: the first is the increase that occurs at high latitudes between 70 and 80°S during the southern summer ($L_s = 250 - 285°$); the second is

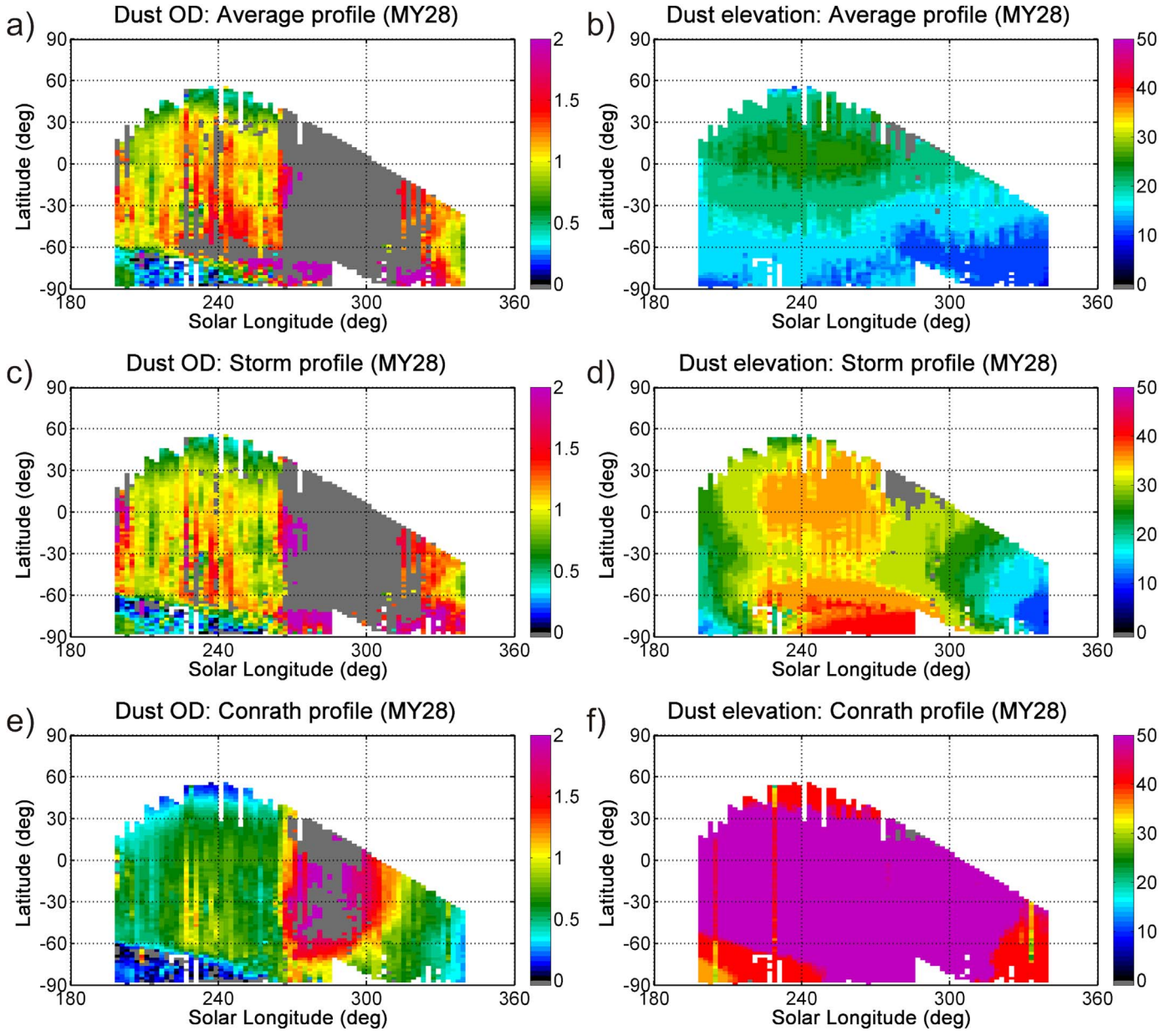

Fig. 14. Retrieved dust optical depth (left) and profile elevation in km (right) corresponding to the different *a priori* altitude profiles tested: (top) MCD climatological average profiles (MCD Scenario 1, used nominally in this work); (middle) MCD storm profiles (MCD Scenario 5); and (bottom) Conrath profile of parameter $\gamma = 0.007$. By dust elevation we mean the elevation at which the dust profile reaches 98% of its total OD (integrated from the ground). The altitude corresponds actually to the bottom altitude of the layer in which that condition is reached (the layers are 5 km thick from 10 to 40 km and 10 km thick at higher altitudes). The optical depth displayed is scaled at 6.1 mbar to remove the topography effect.

observed around 30°N and $L_s = 230°$. Both cases were found to be an artefact due to high dust opacity.[5]

Another noticeable feature is the increase of O_3 column that occurs at low latitudes between $L_s = 45 - 100°$ and which was observed in other previous works (Perrier et al., 2006; Clancy et al., 2016) and reproduced by the models as a relatively important ozone layer present in altitude, between 30 and 60 km (Lebonnois et al., 2006; Lefèvre et al., 2004, 2008).

The retrieved ozone column depends on the aerosol loading in the atmosphere (quantity and altitude profile). As mentioned before, we suspect to have shortcomings in our dust modelling which impacts the quantitative comparison with other results. However, some partial comparisons were performed to estimate the agreement with previous studies.

The comparison with MARCI results (Clancy et al., 2016) shows a qualitative agreement in the different seasonal patterns mentioned above. On the quantitative point of view, comparing the seasonal distribution maps, SPICAM and MARCI seems in reasonable agreement: especially for the northern high latitude ozone between L_s=315–90° and the low latitude increase between L_s= 45–100°. Higher values seems to be retrieve with SPICAM at the edge of the southern polar cap between L_s=0–210° and also for the northern high latitude ozone between L_s=150–200°. However, a more adequate quantitative analysis has to be performed as ozone variations can occur relatively quickly, especially at the pole where its distribution follows the polar vortex waves (Clancy et al., 2016). About hundred simultaneous and co-located SPICAM-MARCI measurements (± 3 h time and ± 1° lat-lon)

[5] It is obvious by visual check that the fit has not worked for these cases which spectra do not show the ozone signature. These spectra have been measured in relatively important dust loading and with a high solar zenith angles (>60°), which increase the airmass and the slant opacity of dust, reducing therefore the impact of ozone absorption in the spectra. Large ozone quantities were inadequately used here by the inversion to lower the signal and reduce the residual.

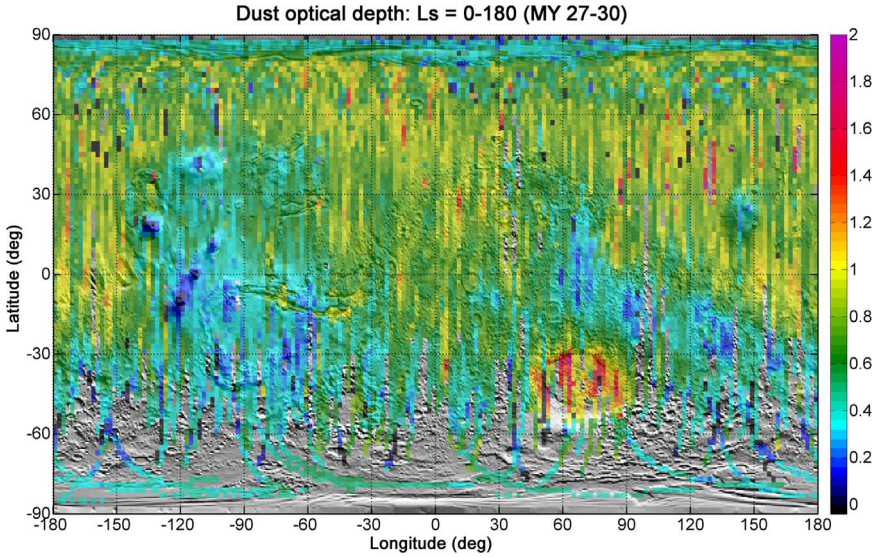

Fig. 15. Composite spatial distribution of the dust optical depth for the aphelion period (L_s=0–180°). The map is averaged on a 2° × 2° grid and was obtained for the complete dataset (MY27-30). Darkened pixels indicates the measurement coverage and the colour scale ranging from dark blue to red corresponds to the retrieved dust opacity. No scaling was performed on the optical depths. (For interpretation of the references to color in this figure legend, the reader is referred to the web version of this article.)

Table 2
Summary of the inversion error on dust OD retrieval.

Conditions	Error
In general	~10%
– During ACB maximum – Above polar caps with low DOD	15–40%
Thin clouds presence ($\tau_c \sim 0.05$)	~15–20%

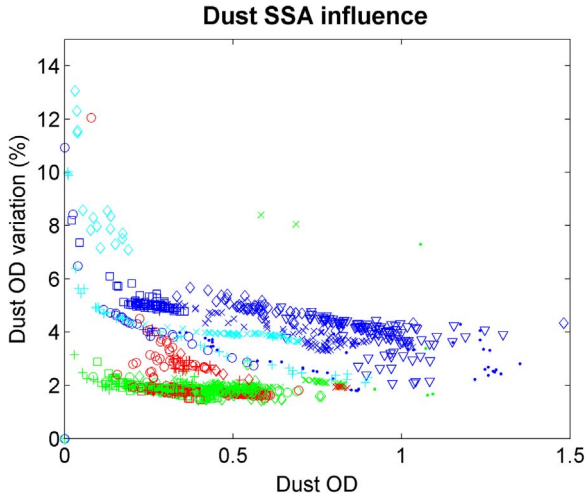

Fig. 16. Influence of the dust SSA on the retrieved dust opacity. The "y" axis shows the variation of retrieved DOD when using the SSA of the 1.8 μm particle size set instead of the nominal 1.6 μm set (both from Wolff et al. (2010)). The "x" axis represents the retrieved COD (nominal). The different markers represent the orbits (cf. Fig. 10). The colours represent the presence of ice surface or cloud: no cloud nor ice in blue, thin cloud ($\tau_c \leq 0.1$) in green, thick cloud ($\tau_c > 0.1$) in red and ice in cyan. (For interpretation of the references to color in this figure legend, the reader is referred to the web version of this article.)

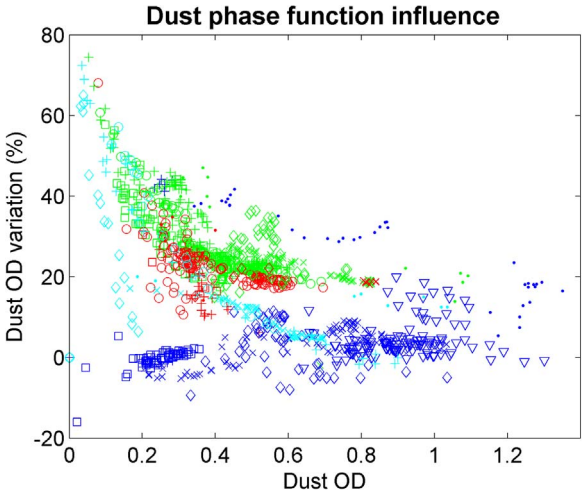

Fig. 17. Influence of the dust phase function on the retrieved dust opacity. The "y" axis shows the variation of retrieved DOD when using the PF as in Mateshvili et al. (2007a) instead of the nominal PF (from Wolff et al. (2010)). The "x" axis represents the retrieved COD (nominal). The different markers represent the orbits (cf. Fig. 10). The colours represent the presence of ice surface or cloud: no cloud nor ice in blue, thin cloud ($\tau_c \leq 0.1$) in green, thick cloud ($\tau_c > 0.1$) in red and ice in cyan. (For interpretation of the references to color in this figure legend, the reader is referred to the web version of this article.)

were identified (personal communication with T. Clancy). The comparison is given in Fig. 18: it appears that SPICAM and MARCI follow the same trend for the 70–75°N results with deviation that usually remain within ± 3 μm-atm. While the results obtained at 33–36°S show a important difference with significantly larger SPICAM values.

The spatial distributions are also in qualitative agreement with MARCI's map: the correlation of ozone with topography is observed in our results with larger ozone columns found above area of lower elevation. We can clearly see on Fig. 19 that the high latitude winter ozone (with high abundances) follows the boundary between the northern lowlands and the southern highlands and higher columns are also observed in the deep basins (Hellas and Argyre) of the southern hemisphere.

A partial comparison with the work of Perrier et al. (2006), which obtained the first ozone results with SPICAM, was also performed. The two sets also show a qualitative agreement of their seasonal trends, but some quantitative differences are reported. The main differences seems to occur when clouds are present and which were not taken into account in Perrier et al. (2006): For the large ozone columns observed at high latitude in the winter hemisphere, when no clouds are present, we generally observe an reasonable agreement between the retrieved

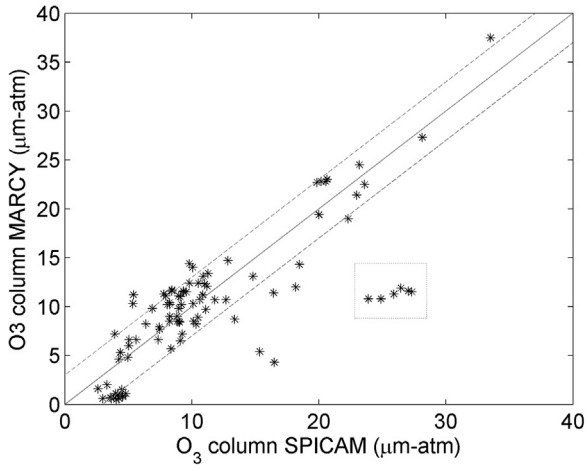

Fig. 18. Comparison of the retrieved ozone column between MARCI and SPICAM. The comparison is made between simultaneous and co-located measurements (± 3 h time and ± 1° lat-lon). These measurements have been recorded between $L_s = 0 - 90°$, and almost all of them were located between 70 and 75°N except the 6 points surrounded by the dotted rectangle which were obtained between 33 and 36°S (around $L_s = 45°$). The $x = y$ line is also represented for an easier comparison.

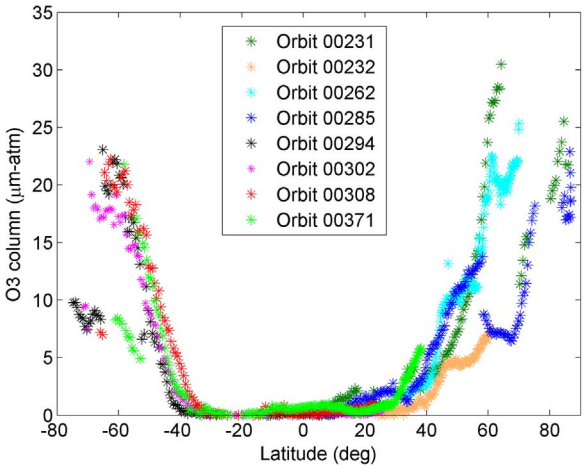

Fig. 20. Retrieved ozone column for several orbits between $L_s = 0 - 30°$ of MY27. Low ozone quantities are observed at low latitude and start to increase at mid-latitude. towards the poles. The transition from ice cloud above a regolith surface to ice surface with no cloud is well visible and marked by a sharp and discontinue decrease, it occurs: around 64°N for orbit 231; after 58°N for orbit 285; and in the four orbits reaching the south pole (around 70°S, 65°S, 65°S and 53°S for orbits 302, 294,308 and 371 respectively).

ozone values of the two sets. On the contrary, when a cloud is present, we often notice a significant increase (which can reach a factor 2) of our retrieved ozone values compared to those of the old set. Incidentally, the transition between the retrieval cases of an ice cloud above regolith and ice cap with no cloud is marked by a steep and discontinuous decrease of the ozone quantity an is shown in Fig. 20. We will have to consider this issue to obtain a smoother transition by introducing a case in which both clouds and ice surface coexist.

If we consider the low latitude ozone (with low abundances), the results show generally a good agreement between the two sets and do not appear to be much affected by the presence of clouds.

4.3.2. Degree of freedom, error and uncertainty

The DoF for the retrieved ozone column is usually larger than 0.8, meaning that the results come from the measurements. The retrieval error on the ozone total column varies generally depending on the season and location. The retrieval error is summarised in Table 3.

The error provided here does not take account of the uncertainties on the assumptions such as the altitude distribution. We have performed some sensitivity tests to estimate the impact of the altitude distribution on the retrieved O_3 column: we have compared the use of MCD v5.0 ozone profiles (nominal in this work) with a constant volume mixing ratio (vmr) profile, resulting in a O_3 column variation between $[-40\%, +30\%]$ for low ozone quantities (< 2 μm-atm) and a decrease between 10% and 60% for larger ozone column. From the convergence

Table 3
Summary of the inversion error on ozone column retrieval.

Conditions	Error
Above polar caps (highest ozone columns)	~5%
Edges of the polar caps	10–20%
Outside polar region (very low ozone columns)	~100%
Low latitude between $L_s = 30 - 100°$ (seasonal max. of the ozone altitude layer)	30–60%

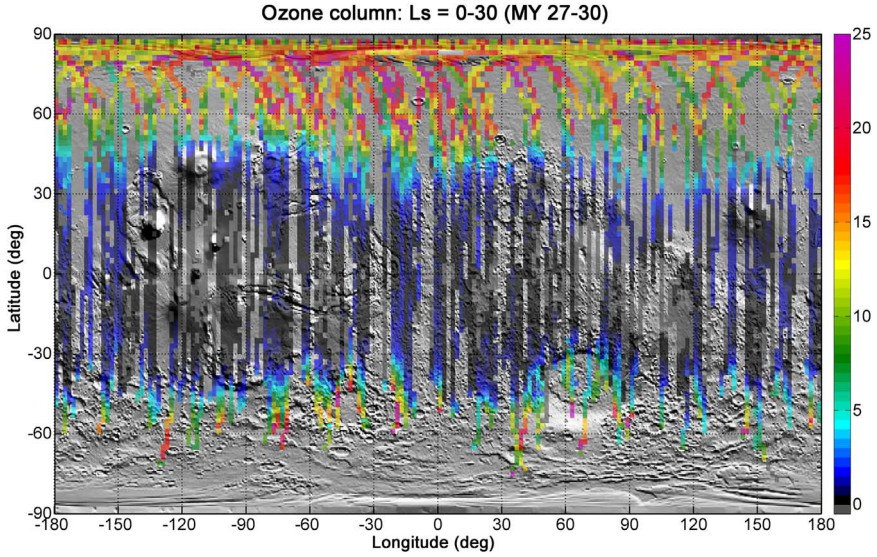

Fig. 19. Spatial distribution of the ozone column (μm-atm) at the beginning of the aphelion period ($L_s = 0 - 30°$).

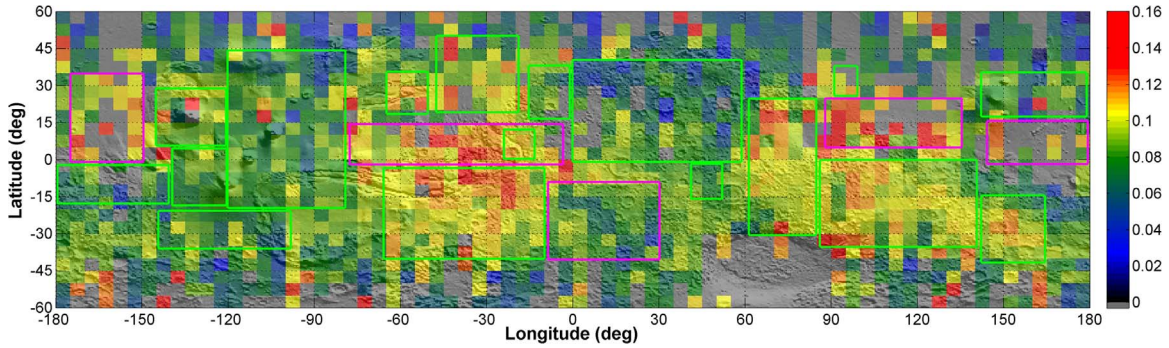

Fig. 21. Map of the surface SSA retrieved at 300 nm in low-to-moderate dust conditions (τ_d < 0.65 and SZA ≤ 60°) between MY27-30. The coloured boxes give a comparison of the relatively large scale reflectance trends with the albedo derived by TES (Christensen et al., 2001). The green boxes represent an anti-correlated trend between TES and SPICAM: i.e. when the area considered is predominantly retrieved "bright" with one of the instrument as the other instrument retrieves it predominantly "dark" (from each instrument albedo range point of view). The magenta boxes represent a correlated trend (i.e. when a predominant "bright" or "dark" area is retrieved with both of the instruments). (For interpretation of the references to color in this figure legend, the reader is referred to the web version of this article.)

point of view, it shows little impact for O_3 column <4 μm-atm with $|\Delta RMS| < \pm 0.001$ and an improved convergence with the constant vmr profile for larger ozone quantities ($\Delta RMS = 0.001 - 0.006$). We have also compared with the results obtained by using the profiles from the previous MCD version v4.3 (dust is also concerned), resulting in variations between $[-50, +30]$%. These results show that altitude distribution can have an important impact on the retrieved ozone column.

4.4. Surface albedo

The results for the regular albedo, which is "dark" in the UV, are strongly dependent on the overlaying aerosol layer which occults and limits the impact of surface on the signal recorded in nadir. Fig. 21 shows the retrieval obtained with low-to-moderate dust loading. This map is not perfectly smooth and individual pixels must be considered with caution. However, the map reveals some regional scale trends that can be compared with the albedo obtained by MGS/TES between 0.3 and 2.9 μm (Christensen et al., 2001). An anti-correlation between the visible and the UV albedo is known to occur and is known as the contrast reversal (Thomas and Veverka, 1986). This reversal is also observed by CRISM (Wolff et al., 2014).

The comparison exhibits a majority of regions where the TES and SPICAM retrieved albedos are anti-correlated such as: 1) in the Tharsis region going from Olympus Mons to Lunae Planum, and East of Arabia Terra, where the TES albedo is very high while SPICAM's ranges from moderate to low; and 2) on the highlands located North and East of Hellas going from Syrtis Major to Terra Cimmera, but also in Chryse Planitia and in the region North of Argyre, where the TES albedo is very low while the SPICAM finds moderate-to-high SSA values.

The comparison also reveals some areas that show correlations such as: 1) in Amazonis Planitia, in the region above the Equator between [80–5°W] and also in the lowlands going from Isidis to Elysium Planitias, where both TES and SPICAM retrieve albedo that ranges from moderate to high values; and 2) in the area South of Valles Marineris between [20–40°S] and in the region West to Hellas between [10°W–30°E], where both TES and SPICAM find albedo corresponding to moderate to low values.

5. Summary and conclusions

We have developed an algorithm to analyse quantitatively Martian nadir spectra recorded in the ultraviolet. It is capable to simultaneously retrieve several parameters of the Martian atmosphere and surface: the dust optical depth, the ozone column but also the cloud opacity or the surface albedo, depending on the cloud presence. The retrieval routine couples the use of the existing complete radiative transfer code LIDORT (Spurr et al., 2001) and the optimal estimation method (Rodgers, 2000). The working principle of our algorithm was described in this paper. The parametrisation used to model the required interactions (absorption, scattering, reflection) between the Martian atmosphere/surface and the solar UV radiation was also detailed and uses more recent references compared to previous works of Perrier et al. (2006), Mateshvili et al. (2007b) and Mateshvili et al. (2009) based on SPICAM/UV. The principle of the cloud detection algorithm included in our retrieval method was explained here and will be described in more detail in a next paper (in preparation) dedicated to the analysis of our cloud retrievals which will also include a comparison with the cloud index of MEX/OMEGA.

The present retrieval method was applied on more than 4 Martian years of SPICAM/UV measurements. The results of the retrievals have been used to derive climatologies of ozone, dust, clouds and surface albedo. These climatologies, which cover a longer period (at least twice) than the previous SPICAM/UV works of Perrier et al. (2006) and Mateshvili et al. (2009), are useful to analyse their spatial and seasonal distributions. We have presented an overview of the seasonal and spatial distributions for each retrieved parameter.

The dust climatology is qualitatively consistent with the results of previous works as Smith (2004), Smith (2009) and Montabone et al. (2015), reproducing the expected spatial and seasonal distributions. The analysis of 4 MYs of data allowed us to highlight the relatively repeatable pattern of the aphelion season, but also the more "variable" perihelion season during which dust storms were observed at different L_s and locations and with variable spatial scales or durations. This distribution shows a good agreement with Montabone et al. (2015). However, relatively large gaps are observed in our retrieval when the dust loading become very large. Also, the quantitative comparisons with the MER (Lemmon et al., 2015) and CRISM (related to Wolff et al. (2009)), show that the dust ODs obtained in this work are generally larger than the results from other works. We have identified possible shortcomings in our dust modelling that are probably (partially) responsible for these discrepancies: the altitude loading profile and the use of a unique particle size to derive the dust optical properties.

An overview of the cloud climatology was also presented, illustrating the different cloud features observed along the year. However, a detailed analysis of the cloud climatology was left for a future paper (in preparation). Nonetheless, some comparisons of the seasonal and spatial trends of these clouds was preformed with results derived in other studies: with Smith (2009) for the aphelion cloud belt; with Benson et al. (2010) and Benson et al. (2011) for the polar hoods; and with Benson et al. (2006) for clouds over the largest volcanoes; which all show generally a qualitative agreement with our results.

An overview of our obtained climatology for ozone was presented and shows that it is generally consistent with the previous SPICAM results (Perrier et al., 2006) or MARCI's one (Clancy et al., 2016). Some partial quantitative comparison also shown a reasonable agreement

with the two datasets. As shown, the retrieval of ozone is influenced by the aerosols presence. The mentioned future improvements in our aerosol modelling will probably change the ozone retrievals.

The retrieval error which is based on the measurement error, was provided for each of these species. The calculation of this error does not include the uncertainty on assumptions such as the altitude distributions, the single scattering albedo or the phase function. We have therefore performed sensitivity tests to quantify the impact on the retrieved quantities when using different altitude profiles or different scattering properties as used in the previous work of Perrier et al. (2006), Mateshvili et al. (2007b) and Mateshvili et al. (2007a) based on SPICAM/UV. We have shown that important variations on the retrieved quantities could stem from the use of these different assumptions, especially with the phase function for clouds and dust and with the altitude distribution for dust and ozone. It is therefore important to use the most accurate properties and distributions to obtain the most reliable retrievals.

The development of our algorithm is also part of the preparation for the NOMAD, an instrument on board of the ExoMars Trace Gas Orbiter that will arrive around Mars in October 2016. The algorithm code will be adapted to analyse the future data from the NOMAD/UVIS channel in order to pursue the monitoring of ozone, dust and cloud distributions.

Acknowledgements

The research program was supported by the Belgian Federal Science Policy Office and the European Space Agency (ESAPRODEX Program -C 90323, 90113, C 4000107727). The research was performed as part of the Interuniversity Attraction Poles program financed by the Belgian Government (Planet TOPERS) and a BRAIN research grant BR/143/A2/SCOOP. The research leading to these results has received funding from the European Community's Seventh Framework Programme (FP7/2007-2013) under the grant agreement no. 607177 CrossDrive and from the European Union's Horizon 2020 Programme (H2020-Compet-08-2014) under grant agreement UPWARDS-633127. We also would like to thank Michael Smith and an anonymous reviewer for their constructive comments and suggestions which helped to improve the present manuscript.

References

Benson, J.L., Bonev, B.P., James, P.B., Shan, K.J., Cantor, B.A., Caplinger, M.A., 2003. The seasonal behavior of water ice clouds in the Tharsis and Valles Marineris regions of Mars: Mars Orbiter Camera observations. Icarus 165, 34–52.

Benson, J.L., James, P.B., Cantor, B.A., Remigio, R., 2006. Interannual variability of water ice clouds over major martian volcanoes observed by MOC. Icarus 184, 365–371.

Benson, J.L., Kass, D.M., Kleinböhl, A., McCleese, D.J., Schofield, J.T., Taylor, F.W., 2010. Mars' south polar hood as observed by the Mars climate sounder. J. Geophys. Res. (Planets) 115, 12015.

Benson, J.L., Kass, D.M., Kleinböhl, A., 2011. Mars' north polar hood as observed by the Mars Climate Sounder. J. Geophys. Res. (Planets) 116, 3008.

Bertaux, J.L., Korablev, O., Perrier, S., Quémerais, E., Montmessin, F., Leblanc, F., Lebonnois, S., Rannou, P., Lefèvre, F., Forget, F., Fedorova, A., Dimarellis, E., Reberac, A., Fonteyn, D., Chaufray, J.Y., Guibert, S., 2006. SPICAM on Mars Express: Observing modes and overview of UV spectrometer data and scientific results. J. Geophys. Res. (Planets) 111, 10.

Brion, J., Chakir, A., Daumont, D., Malicet, J., Parisse, C., 1993. High-resolution laboratory absorption cross section of O_3. Temp. Eff. Chem. Phys. Lett. 213, 610–612.

Byrne, S., Zuber, M.T., Neumann, G.A., 2008. Interannual and seasonal behavior of Martian residual ice-cap albedo. Planet. Space Sci. 56, 194–211.

Cantor, B.A., James, P.B., Caplinger, M., Wolff, M.J., 2001. Martian dust storms: 1999 Mars Orbiter Camera observations. J. Geophys. Res. 106, 23653–23688.

Chandrasekhar, S., 1960. Radiative transfer.

Christensen, P.R., Bandfield, J.L., Hamilton, V.E., Ruff, S.W., Kieffer, H.H., Titus, T.N., Malin, M.C., Morris, R.V., Lane, M.D., Clark, R.L., Jakosky, B.M., Mellon, M.T., Pearl, J.C., Conrath, B.J., Smith, M.D., Clancy, R.T., Kuzmin, R.O., Roush, T., Mehall, G.L., Gorelick, N., Bender, K., Murray, K., Dason, S., Greene, E., Silverman, S., Greenfield, M., 2001. Mars Global Surveyor Thermal Emission Spectrometer experiment: Investigation description and surface science results. J. Geophys. Res. 106, 23823–23872.

Clancy, R.T., Grossman, A.W., Wolff, M.J., James, P.B., Rudy, D.J., Billawala, Y.N., Sandor, B.J., Lee, S.W., Muhleman, D.O., 1996. Water vapor saturation at low altitudes around Mars Aphelion: a key to Mars climate? Icarus 122, 36–62.

Clancy, R.T., Sandor, B.J., Wolff, M.J., Christensen, P.R., Smith, M.D., Pearl, J.C., Conrath, B.J., Wilson, R.J., 2000. An intercomparison of ground-based millimeter, MGS TES, and Viking atmospheric temperature measurements: seasonal and interannual variability of temperatures and dust loading in the global Mars atmosphere. J. Geophys. Res. 105, 9553–9572.

Clancy, R.T., Wolff, M.J., Christensen, P.R., 2003. Mars aerosol studies with the MGS TES emission phase function observations: optical depths, particle sizes, and ice cloud types versus latitude and solar longitude. J. Geophys. Res. (Planets) 108, 5098.

Clancy, R.T., Wolff, M.J., Lefvre, F., Cantor, B.A., Malin, M.C., Smith, M.D., 2016. Daily global mapping of Mars ozone column abundances with MARCI UV band imaging. Icarus 266, 112–133.

Conrath, B.J., 1975. Thermal structure of the Martian atmosphere during the dissipation of the dust storm of 1971. Icarus 24, 36–46.

Fedorova, A., Korablev, O., Bertaux, J.L., Rodin, A., Kiselev, A., Perrier, S., 2006. Mars water vapor abundance from SPICAM IR spectrometer: seasonal and geographic distributions. J. Geophys. Res. (Planets) 111, 9.

Forget, F., Hourdin, F., Fournier, R., Hourdin, C., Talagrand, O., Collins, M., Lewis, S.R., Read, P.L., Huot, J.P., 1999. Improved general circulation models of the Martian atmosphere from the surface to above 80 km. J. Geophys. Res. 104, 24155–24176.

Gorshelev, V., Serdyuchenko, A., Weber, M., Chehade, W., Burrows, J.P., 2014. High spectral resolution ozone absorption cross-sections – Part 1: measurements, data analysis and comparison with previous measurements around 293 K. Atmos. Meas. Tech. 7, 609–624.

Hale, A.S., Bass, D.S., Tamppari, L.K., 2005. Monitoring the perennial martian northern polar cap with MGS MOC. Icarus 174, 502–512.

Hansen, G.B., 1999. Control of the radiative behavior of the Martian polar caps by surface CO_2 ice: evidence from Mars Global Surveyor measurements. J. Geophys. Res. 104, 16471–16486.

Hapke, B., 2005. Theory of reflectance and emittance spectroscopy. In: Topics in 880 Remote Sensing, Cambridge University Press.

Hartmann, W.K., 1978. Mars - Topographic control of clouds, 1907–1973. Icarus 33, 380–387.

Ityaksov, D., Linnartz, H., Ubachs, W., 2008. Deep-UV absorption and Rayleigh scattering of carbon dioxide. Chem. Phys. Lett. 462, 31–34.

James, P.B., Bonev, B.P., Wolff, M.J., 2005. Visible albedo of Mars' south polar cap: 2003 HST observations. Icarus 174, 596–599.

Karaiskou, A., Vallance, C., Papadakis, V., Vardavas, I.M., Rakitzis, T.P., 2004. Absolute absorption cross-section measurements of CO_2 in the ultraviolet from 200 to 206 nm at 295 and 373 K. Chem. Phys. Lett. 400, 30–34.

Kieffer, H.H., 1990. H2o grain size and the amount of dust in Mars' residual north polar cap. J. Geophys. Res.: Solid Earth 95, 1481–1493.

Kleinböhl, A., Schofield, J.T., Kass, D.M., Abdou, W.A., Backus, C.R., Sen, B., Shirley, J.H., Lawson, W.G., Richardson, M.I., Taylor, F.W., Teanby, N.A., McCleese, D.J., 2009. Mars Climate Sounder limb profile retrieval of atmospheric temperature, pressure, and dust and water ice opacity. J. Geophys. Res. (Planets) 114, E10006.

Langevin, Y., Bibring, J.P., Montmessin, F., Forget, F., Vincendon, M., Douté, S., Poulet, F., Gondet, B., 2007. Observations of the south seasonal cap of Mars during recession in 2004–2006 by the OMEGA visible/near-infrared imaging spectrometer on board Mars Express. J. Geophys. Res. (Planets) 112, 8.

Lebonnois, S., Quémerais, E., Montmessin, F., Lefèvre, F., Perrier, S., Bertaux, J.L., Forget, F., 2006. Vertical distribution of ozone on Mars as measured by SPICAM/Mars Express using stellar occultations. J. Geophys. Res. (Planets) 111, 9.

Lefèvre, F., Lebonnois, S., Montmessin, F., Forget, F., 2004. Three-dimensional modeling of ozone on Mars. J. Geophys. Res. (Planets) 109, 7004.

Lefèvre, F., Bertaux, J.L., Clancy, R.T., Encrenaz, T., Fast, K., Forget, F., Lebonnois, S., Montmessin, F., Perrier, S., 2008. Heterogeneous chemistry in the atmosphere of Mars. Nature 454, 971–975.

Lemmon, M.T., Wolff, M.J., Bell III, J.F., Smith, M.D., Cantor, B.A., Smith, P.H., 2015. Dust aerosol, clouds, and the atmospheric optical depth record over 5 Mars years of the Mars Exploration Rover mission. Icarus 251, 96–111.

Madeleine, J.B., Forget, F., Millour, E., Montabone, L., Wolff, M.J., 2011. Revisiting the radiative impact of dust on Mars using the LMD Global Climate Model. J. Geophys. Res. (Planets) 116, 11010.

Madeleine, J.B., Forget, F., Spiga, A., Wolff, M.J., Montmessin, F., Vincendon, M., Jouglet, D., Gondet, B., Bibring, J.P., Langevin, Y., Schmitt, B., 2012. Aphelion water-ice cloud mapping and property retrieval using the OMEGA imaging spectrometer onboard Mars Express. J. Geophys. Res. (Planets) 117, 0.

Malicet, J., Daumont, D., Charbonnier, J., Parisse, C., Chakir, A., Brion, J., 1995. Ozone UV spectroscopy. II. Absorption cross-sections and temperature dependence. J. Atmos. Chem. 21, 263–273.

Marcq, E., Belyaev, D., Montmessin, F., Fedorova, A., Bertaux, J.L., Vandaele, A.C., Neefs, E., 2011. An investigation of the SO_2 content of the venusian mesosphere using SPICAV-UV in nadir mode. Icarus 211, 58–69.

Mateshvili, N., Fussen, D., Vanhellemont, F., Bingen, C., Dodion, J., Montmessin, F., Perrier, S., Bertaux, J.L., 2007a. Detection of Martian dust clouds by SPICAM UV nadir measurements during the October 2005 regional dust storm. Adv. Space Res. 40, 869–880.

Mateshvili, N., Fussen, D., Vanhellemont, F., Bingen, C., Dodion, J., Montmessin, F., Perrier, S., Dimarellis, E., Bertaux, J.L., 2007b. Martian ice cloud distribution obtained from SPICAM nadir UV measurements. J. Geophys. Res. (Planets) 112, 7004.

Mateshvili, N., Fussen, D., Vanhellemont, F., Bingen, C., Dekemper, E., Loodts, N., Tetard, C., 2009. Water ice clouds in the Martian atmosphere: two Martian years of SPICAM nadir UV measurements. Planet. Space Sci. 57, 1022–1031.

McClintock, W.E., Rottman, G.J., Woods, T.N., 2005. Solar-Stellar Irradiance Comparison

Experiment II (Solstice II): instrument concept and design. Sol. Phys. 230, 225–258.
Mishchenko, M.I., Travis, L.D., Mackowski, D.W., 1996. T-matrix computations of light scattering by nonspherical particles: a review. J. Quant. Spectrosc. Radiat. Transf. 55, 535–575.
Montabone, L., Forget, F., Millour, E., Wilson, R.J., Lewis, S.R., Cantor, B., Kass, D., Kleinböhl, A., Lemmon, M.T., Smith, M.D., Wolff, M.J., 2015. Eight-year climatology of dust optical depth on Mars. Icarus 251, 65–95.
Navarro, T., Forget, F., Millour, E., Greybush, S.J., 2014. Detection of detached dust layers in the Martian atmosphere from their thermal signature using assimilation. Geophys. Res. Lett. 41, 6620–6626.
Perrier, S., Bertaux, J.L., Lefèvre, F., Lebonnois, S., Korablev, O., Fedorova, A., Montmessin, F., 2006. Global distribution of total ozone on Mars from SPICAM/MEX UV measurements. J. Geophys. Res. (Planets) 111, 9.
Rodgers, C.D., 2000. Inverse methods for atmospheric sounding – theory and practice. Volume 2 of Series on Atmospheric Oceanic and Planetary Physics. World Scientific Publishing Co.
Serdyuchenko, A., Gorshelev, V., Weber, M., Chehade, W., Burrows, J.P., 2014. High spectral resolution ozone absorption cross-sections – Part 2: temperature dependence. Atmos. Meas. Tech. 7, 625–636.
Shemansky, D.E., 1972. CO_2 extinction coefficient 1700–3000 Å. J. Chem. Phys. 56, 1582–1587.
Smith, M.D., 2004. Interannual variability in TES atmospheric observations of Mars during 1999–2003. Icarus 167, 148–165.
Smith, M.D., 2008. Spacecraft observations of the Martian Atmosphere. Annu. Rev. Earth Planet. Sci. 36, 191–219.
Smith, M.D., 2009. THEMIS observations of Mars aerosol optical depth from 2002–2008. Icarus 202, 444–452.
Smith, M.D., Wolff, M.J., Spanovich, N., Ghosh, A., Banfield, D., Christensen, P.R., Landis, G.A., Squyres, S.W., 2006. One Martian year of atmospheric observations using MER Mini-TES. J. Geophys. Res. (Planets) 111, 12.
Smith, M.D., Wolff, M.J., Clancy, R.T., Kleinböhl, A., Murchie, S.L., 2013. Vertical distribution of dust and water ice aerosols from CRISM limb-geometry observations. J. Geophys. Res. (Planets) 118, 321–334.
Sneep, M., Ubachs, W., 2005. Direct measurement of the Rayleigh scattering cross section in various gases. J. Quant. Spectrosc. Radiat. Transf. 92, 293–310.
Spurr, R., 2002. Simultaneous derivation of intensities and weighting functions in a general pseudo-spherical discrete ordinate radiative transfer treatment. J. Quant. Spectrosc. Radiat. Transf. 75, 129–175.
Spurr, R.J.D., 2004. A new approach to the retrieval of surface properties from earthshine measurements. J. Quant. Spectrosc. Radiat. Transf. 83, 15–46.
Spurr, R.J.D., Kurosu, T.P., Chance, K.V., 2001. A linearized discrete ordinate radiative transfer model for atmospheric remote-sensing retrieval. J. Quant. Spectrosc. Radiat. Transf. 68, 689–735.
Thomas, P., Veverka, J., 1986. Red/violet contrast reversal on Mars - Significance for eolian sediments. Icarus 66, 39–55.
Tomasko, M.G., Doose, L.R., Lemmon, M., Smith, P.H., Wegryn, E., 1999. Properties of dust in the Martian atmosphere from the Imager on Mars Pathfinder. J. Geophys. Res. (Planets) 104, 8987–9008.
Warren, S.G., Brandt, R.E., 2008. Optical constants of ice from the ultraviolet to the microwave: a revised compilation. J. Geophys. Res. (Atmos.) 113, 14220.
Wolff, M.J., Smith, M.D., Clancy, R.T., Arvidson, R., Kahre, M., Seelos, F., Murchie, S., Savijärvi, H., 2009. Wavelength dependence of dust aerosol single scattering albedo as observed by the compact reconnaissance imaging spectrometer. J. Geophys. Res. (Planets) 114.
Wolff, M.J., Clancy, R.T., Goguen, J.D., Malin, M.C., Cantor, B.A., 2010. Ultraviolet dust aerosol properties as observed by MARCI. Icarus 208, 143–155.
Wolff, M.J., Clancy, R.T., Cantor, B., Haberle, R.M., 2014. The MARCI water ice cloud optical depth (Public) database, In: Proceedings of the Fifth International Workshop on the Mars Atmosphere: Modelling and Observations.
Yang, P., Baum, B.A., Heymsfield, A.J., Hu, Y.X., Huang, H.L., Tsay, S.C., Ackerman, S., 2003. Single-scattering properties of droxtals. J. Quant. Spectrosc. Radiat. Transf. 79–80, 1159–1169.